2-2008

Optical Imaging and Spectroscopy of the Galactic Supernova Remnant 3C 58 (G130.7+3.1)

Robert Fesen
Dartmouth College

Gwen Rudie
Dartmouth College

Alan Hurford
Dartmouth College

Aljeandro Soto
Dartmouth College

The Astrophysical Journal Supplement Series, 174:379–395, 2008 February

OPTICAL IMAGING AND SPECTROSCOPY OF THE GALACTIC SUPERNOVA REMNANT 3C 58 (G130.7+3.1)

Robert Fesen, Gwen Rudie, Alan Hurford, and Aljeandro Soto
6127 Wilder Laboratory, Physics and Astronomy Department Dartmouth College, Hanover, NH 03755
Received 2006 August 26; accepted 2007 August 21

ABSTRACT

We present a comprehensive imaging and spectroscopic survey of optical emission knots associated with the young Galactic supernova remnant 3C 58. Hα images show hundreds of clumpy filaments and knots arranged in a complex structure covering a nearly circular area roughly 400″ in diameter. A quite different emission structure is seen in [O III], where the brightest features are less clumpy and largely confined to the remnant's northwest quadrant. Measured radial velocities of over 450 knots reveal two distinct kinematic populations; one with average and peak expansion velocities of 770 and 1100 km s^{-1}, respectively, forming a thick shell, and the other showing $|v| \leq 250$ km s^{-1}. High-velocity knots ($|v| \geq 500$ km s^{-1}) exhibit a strong bipolar expansion pattern with redshifted and blueshifted knots located in northeastern and southwestern regions, respectively. These knots also show strong [N II]/Hα line emission ratios, suggesting enhanced N/H. In contrast, the slower expanding knot population shows much lower [N II]/Hα line ratios and likely represents circumstellar mass loss material from the 3C 58 progenitor. Proper-motion estimates using images spanning a 28 yr time interval suggest positional shifts of between 0.5″ and 2.0″, implying proper motions of 0.02″–0.07″ yr^{-1}. These values agree with previous estimates but are much less than the $\approx$0.2″ yr^{-1} expected if 3C 58 were associated with historic guest star of 1181 CE.

Subject headings: ISM: individual (3C 58) — ISM: kinematics and dynamics — supernova remnants

Online material: color figures, extended figures, machine-readable table

1. INTRODUCTION

The Galactic supernova remnant 3C 58 (G130.7.1+3.1) shares several properties with the Crab Nebula (see Table 1). Although the Crab Nebula is far brighter and more luminous than 3C 58, both remnants exhibit a relatively flat radio continuum ($S_\nu \propto \nu^\alpha$; $\alpha_{\rm Crab} = -0.26$, $\alpha_{\rm 3C\,58} = -0.09$) with regions of high linear polarization. Both are also classified as "plerion" remnants, meaning they are brightest near their centers in both the radio and X-rays (i.e., "filled-center" SNRs; Weiler & Seielstad 1971; Wilson & Weiler 1976).

The defining properties of plerionic or "Crab-like" remnants arise mainly from their young, rapidly spinning central pulsars. The pulsars provide the magnetic field and relativistic particles that generate the observed center-filled synchrotron radiation fields. While a faint central X-ray point source in 3C 58 had long been suspected to be a neutron star (Becker et al. 1982; Helfand et al. 1995), it was only recently identified as a pulsar, first through X-rays ($P = 65.7$ ms, PSR J0205+6449; Murray et al. 2002) and then quickly confirmed in the radio (Camilo et al. 2002; Malofeev et al. 2003).

It has been argued that 3C 58 is a young supernova remnant (SNR) due to a proposed association with a historically reported "guest star," in this case, the apparent SN of 1181 CE (Stephenson 1971; Clark & Stephenson 1997; Liu 1983; Stephenson & Green 2002). If this SN–SNR connection is correct, then 3C 58 is currently 827 yr old, making it nearly 130 yr younger than the Crab Nebula (SN 1054).

Following unsuccessful initial searches for coincident optical emission (Wyndham 1966; Weiler & Seielstad 1971; van den Bergh et al. 1973), faint nebulosity was finally detected in 1977 on deep photographic plates taken using the Palomar 5 m telescope (van den Bergh 1978). The images showed extended remnant emission over an area $\sim$300″ in diameter consisting of short, somewhat diffuse filaments and knots.

Spectra of a few of these filaments situated along the northern limb confirmed them as shock emission (Kirshner & Fesen 1978). Subsequent optical spectra taken of nearly 50 filaments revealed radial velocities from +1000 to −1075 km s^{-1} but also a surprising number of low-velocity knots ($v = \pm 300$ km s^{-1}) located throughout the remnant including near the remnant's center (Fesen 1983; Fesen et al. 1988). These radial velocity measurements lead to an estimated maximum expansion velocity of around $\pm$1000 km s^{-1}, roughly half the Crab's 1500–2500 km s^{-1} expansion velocity (Woltjer 1972; Clark et al. 1983; Fesen & Ketelsen 1985; Lawrence et al. 1995).

With an angular size of $6.3' \times 10.3'$ (Reynolds & Aller 1988) and lying at an estimated distance of $\sim$3 kpc (2.6 kpc, Green & Gull 1982; 3.2 kpc, Roberts et al. 1993), 3C 58 is 6×9.5 pc in size or roughly twice as big as the Crab (3×4 pc). This size together with its relatively low expansion velocity observed creates something of a puzzle. Despite supposedly being 127 yr younger with an expansion velocity only about half that of the Crab, 3C 58 is somehow much larger physically.

If 3C 58 is really only 827 yr old at present (i.e., the remnant of SN 1181), then its age and its observed angular size imply average expansion velocities of 3500–5700 km s^{-1}. Unless significantly decelerated, the remnant should therefore exhibit proper motions as large as 0.20″–0.40″ yr^{-1}. However, reported proper motion measurements indicate much smaller filament motions, 0.05″–0.07″ yr^{-1} (Fesen et al. 1988; van den Bergh 1990). This suggests lower expansion velocities of around 700–1100 d_3 km s^{-1}, but well in line with 3C 58's observed knot radial velocities.

The apparent agreement of the observed proper motions and radial velocities highlights the discrepancy of the remnant's presumed young age based on the historical connection with the 1181 supernova and the remnant's large angular size. This discord is supported by radio observations, which also indicate an average expansion of 0.014% $\pm$ 0.003% yr^{-1}, corresponding to an expansion velocity

TABLE 1
COMPARISON OF 3C 58 WITH THE CRAB NEBULA

Item	Crab Nebula	3C 58	Refs. for Crab Nebula	Refs. for 3C 58
SNR ID	G184.6−5.8	G130.7+3.1	...	...
Assoc. SN event	1054	1181 (?)	1, 2	3, 4, 5
Current age (yr)	953	827 (?)	...	...
Angular size (arcmin)	5×7	6.3×10.3	6	7, 8
Distance (kpc)	∼2	∼3	9	10, 11
Physical size (pc)	3×4	6×9.5	...	...
z distance (pc)	200	150	...	...
$\langle V_{\rm exp}\rangle R/t$ (km s^{-1})	1500–2100	3500–5700	...	...
Max $V_{\rm exp}$ (obs) (km s^{-1})	2200	1100	12, 13, 14	15, 16
α (radio)	−0.26	−0.09	6	8, 17
1 GHz flux (Jy)	1020	33	18	18
$\nu_{\rm break}$ (Hz)	10×10^{12}	0.05×10^{12}	19	19
L (10^7–10^{13} Hz) (ergs s^{-1})	35.7×10^{35}	1.9×10^{34}	20	20
L (0.5–10 keV) (ergs s^{-1})	2.1×10^{37}	1×10^{34}	21	22
$E(B-V)$ (mag)	0.52	0.68	23, 24, 25	26
Peak visual mag.	−18	−13 to −14	5	5

REFERENCES.—(1) Duyvendak 1942; (2) Mayall & Oort 1942; (3) Stephenson 1971; (4) Clark & Stephenson 1977; (5) Stephenson & Green 2002; (6) Wilson 1972; (7) Wilson & Weiler 1976; (8) Reynolds & Aller 1988; (9) Davidson & Fesen 1985; (10) Green & Gull 1982; (11) Roberts et al. 1993; (12) Clark et al. 1983; (13) Fesen & Ketelsen 1985; (14) Lawrence et al. 1995; (15) Fesen et al. 1988; (16) this paper; (17) Green 1986; (18) Green 2004; (19) Green 1994; (20) Ivanov et al. 2004; (21) Toor & Seward 1974; (22) Torii et al. 2000; (23) Wu 1981; (24) Blair et al. 1992; (25) Sollerman et al. 2000; (26) Fesen et al. 1988.

of 630 km s^{-1} along the major axis (Bietenholz et al. 2001; Bietenholz 2006).

Becker et al. (1982) proposed solving this size versus expansion velocity problem by simply abandoning the proposed historical association of 3C 58 with SN 1181. Chevalier (2004, 2005) has also argued that 3C 58 is likely much older, around 2400 ± 500 yr, based on the observed properties of the pulsar's wind nebula. A much older remnant might also resolve the unexpectedly low surface temperature for the 3C 58 pulsar, which has a temperature well below the standard NS cooling curve predictions for an age of 1000 yr (Slane et al. 2002; Yakovlev et al. 2002; Page et al. 2004).

An alternative solution is that 3C 58's ejecta underwent a rapid deceleration due to a relatively dense ambient medium (van den Bergh 1990; Bietenholz et al. 2001). Evidence in favor of this scenario may be the presence of low-velocity, possibly N-rich circumstellar material observed throughout much of the remnant (Fesen et al. 1988). However, such strong and rapid deceleration would appear unlikely given the lack of any appreciable radio emission from an outer supernova shell of ejecta (Bietenholz 2006).

A related proposed solution is that 3C 58's optical filaments result from the interaction of the remnant's expanding pulsar wind nebula and outlying supernova ejecta (Slane et al. 2004). Support for this picture comes from thermal X-ray emission seen in the outer regions of the remnant (Bocchino et al. 2001; Slane et al. 2004). However, such an interaction scenario might lead to an acceleration (rather than a deceleration) of outer ejecta filaments, like that observed in the Crab Nebula (Trimble 1968; Trimble & Rees 1970).

In this paper, we present a comprehensive imaging and spectroscopic survey of the remnant's optical emission knots in order to better define its optical structure and kinematic properties. These data reveal an extensive network of filaments and knots that consists of two distinct expansion velocity populations with similar spectral properties. No radial velocities in excess of 1100 km s^{-1} were found, and we confirm the relatively low proper motion values reported by previous studies. The imaging and spectral observations along with knot radial velocities and flux measurement procedures are described in § 2 with the results presented and discussed in §§ 3 and 4, respectively.

2. OBSERVATIONS

2.1. *Imaging*

Interference filter images of 3C 58 were obtained in 1994 September using a Loral front-side illuminated 2048×2048 CCD detector and a backside illuminated 1024×1024 Tektronics detector attached to the McGraw-Hill 1.3 m telescope at the MDM Observatory at Kitt Peak. The Loral CCD was binned 2×2 resulting in an image scale of 0.635″ and a field of view of 10.8′ square. The Tektronics CCD had an image scale of 0.508″ and a field of view of 8.6′ square.

Deeper and higher resolution images were obtained in 1996 using the 1024×1024 Tektronix CCD detector attached to the MDM Hiltner 2.4 m telescope. The 2.4 m telescope-camera system produced a 4.7′ square field of view with 0.275″ pixels. For these smaller field of view images, the remnant was divided into four quadrants (NE, SE, NW, and SW) for imaging.

A variety of filters were used that would allow for the detection of emission lines at both large positive and negative radial velocities. The chosen filters were also fairly narrow in passband to detect the fainter emission features. The 1.3 m telescope image data included: Hα filter images ($\lambda_c = 6565$ Å; FWHM = 90 Å) sensitive to Hα and [N II] $\lambda\lambda$6548, 6583 emitting knots with low to moderate radial velocity ($v_r = \pm 2000$ km s^{-1}), a 6450 Å filter (FWHM = 90 Å) sensitive to highly negative velocity Hα and [N II] emitting ejecta ($v_r = -4000$ to -7500 km s^{-1}, a broad 6650 filter (FWHM = 250 Å) to detect both [S II] $\lambda\lambda$6716, 6731 emission knots with $v_r = -4000$ to +3000 km s^{-1} and [N II] knots with large positive velocities ($v_r = +1000$ to +8500 km s^{-1}), a [O III] λ5007 filter (FWHM = 90 Å), and a standard R-band filter to serve as a reference on stellar sources in each field. Total exposure times were typically 3000 s. The 1996 2.4 m telescope images were taken through the Hα and off-band ($\lambda_c = 6450$ Å) filters and consisted of two 800 s exposures in each filter for the four image regions.

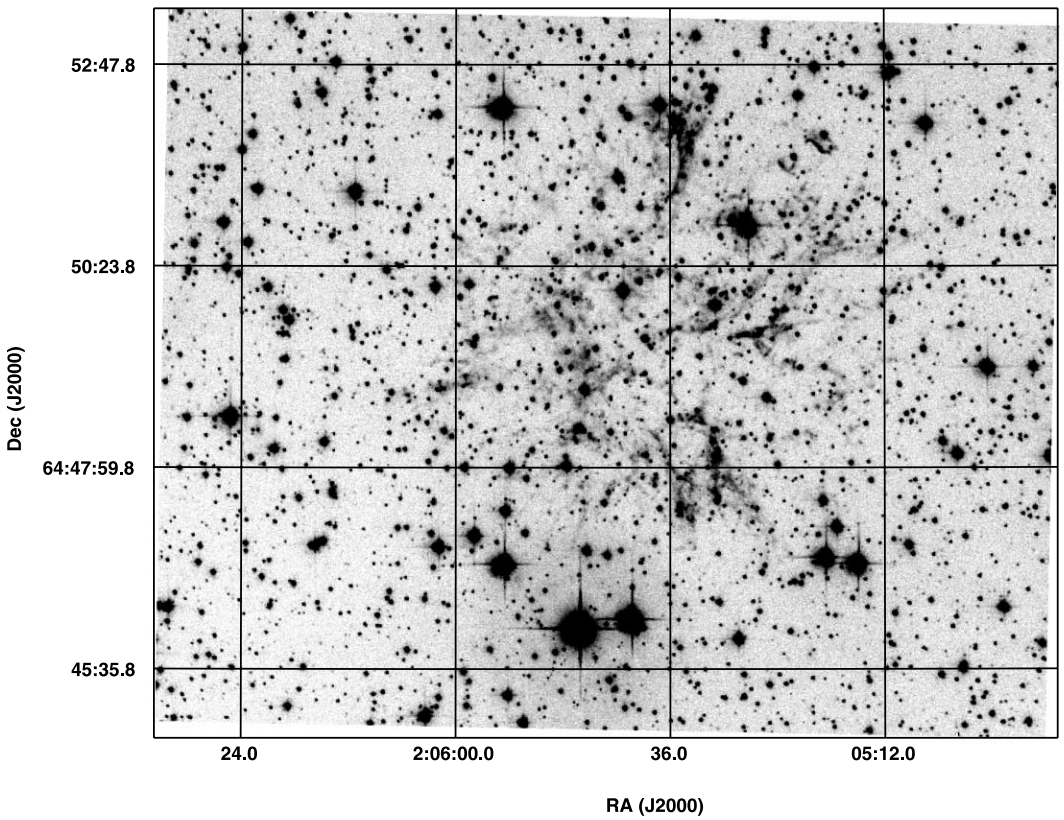

FIG. 1.—The 3C 58 remnant shown in Hα + [N II] emission. The image shown covers a $10.5' \times 8.4'$ field of view.

A set of Hα filter images (FWHM = 90 Å) were also taken on 2005 October 6 with the MDM 2.4 m telescope in order to measure proper motions of the remnant's emission features. A 2048×2048 Tektronix CCD detector was used with $0.275''$ pixels and an effective $7.5' \times 7.5'$ field of view. Three 600 s exposures were taken in fair seeing (FWHM = $1.2''$) and nonphotometric conditions.

2.2. *Long-Slit Spectra*

Low-dispersion, long-slit optical spectra of 3C 58 were obtained on 1995 October 16–23 using the MDM 2.4 m telescope with the Modular Spectrograph and a 1024×1024 Tektronix CCD detector. A $2.0'' \times 6.3'$ slit and a 1200 lines mm^{-1}, 5800 Å blaze grating providing a dispersion of 2.34 Å pixel^{-1}. At each slit position we obtained sets of two or three 1000–1200 s exposures spanning the spectral region 4600–7000 Å with an effective spectral resolution of $\simeq$8 Å.

Although spectra were obtained on seven nights, the data for the first three nights were of poor quality. The four usable nights' data were reduced using IRAF routines and calibrated with Hg, Ne, and Xe lamps and spectrophotometric standard stars (Oke 1974; Stone 1977; Massey & Gronwall 1990).

Six to twelve slit positions were observed during each of the four good quality nights (i.e., nights 4 through 7), yielding 1 to 22 knot spectra per slit position. Slit positions are identified with a number indicating the night on which the data were taken and a letter (capitalized) for each slit position taken that night. Spectra were obtained from a total of 36 slit positions with 463 individual emission knots measured. Each knot was assigned a letter associated with its sequential position along the slit. (Note: Precise slit and knot positions are shown in Fig. 26.)

Individual knot spectra were extracted from the two-dimensional data and radial velocities and relative line fluxes were measured. Radial velocity measurements are biased toward the [N II] $\lambda\lambda$6583, 6548 lines due to their greater observed emission strength. Determination of knot positions was accomplished by comparing the two-dimensional spectra with our 2.4 m Hα image of the remnant.

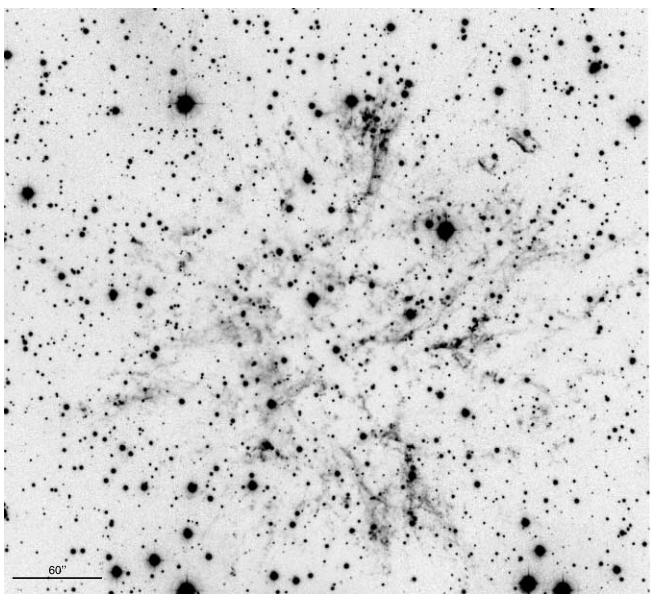

FIG. 2.—Higher resolution image of the central region of the 3C 58 remnant in Hα emission.

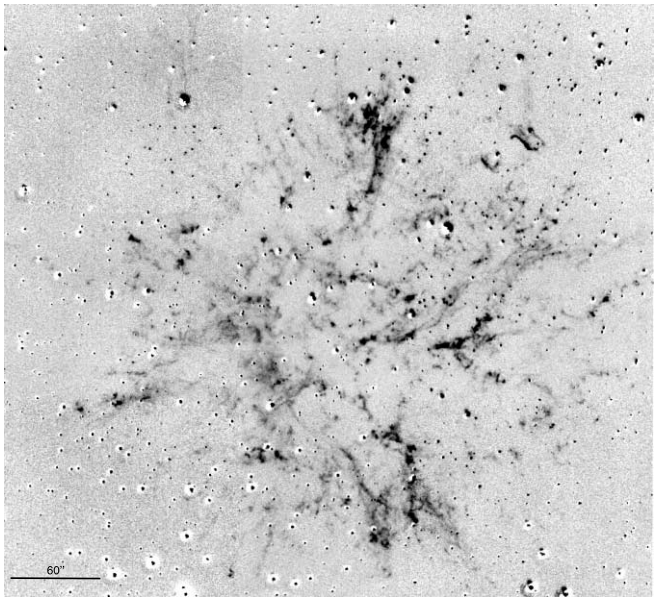

FIG. 3.—Continuum-subtracted version of the Hα image shown in Fig. 2.

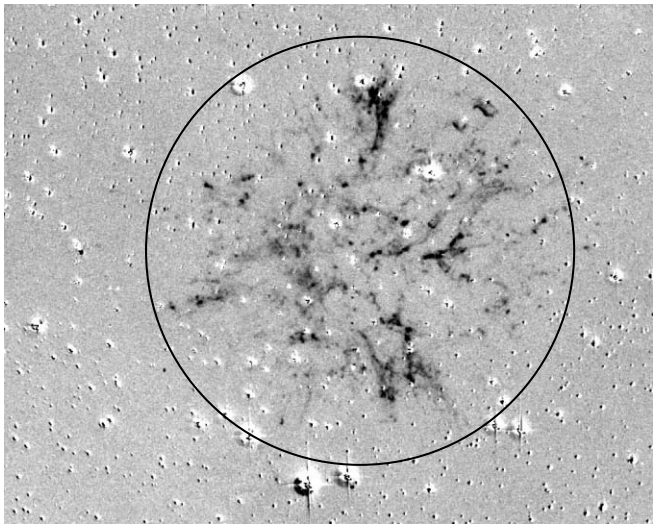

FIG. 4.—Wide Hα image of 3C 58. This shows that the vast majority of Hα emission lies within a radius of 200″ (*circle*). A few exceptions are seen along the far eastern and western limbs, where a few knots are visible farther out. The circle shown here is centered on the position of the remnant's pulsar, PSR J0205+6449 [α(J2000.0) = $02^h05^m37.92^s$, δ(J2000.0) = $64^\circ49'42.8''$; Camilo et al. 2002].

Radial velocities are believed accurate to ± 75 km s^{-1}, affected as much by the low dispersion as by uncertainties in precise knot locations within the 2″ wide slit. Flux measurement errors can reach 50% also due to uncertainties in knot locations within the slit. Weak residual night sky emissions at [O I] λ5577 and λ6300 due to imperfect sky subtraction were manually removed in some of the final spectra.

3. RESULTS

3.1. *Imaging*

Figure 1 shows a Hα+[N II] image of 3C 58. As can seen in this image, the remnant's emission consists of clumpy filaments and knots arranged in a complex structure covering an area roughly 400″ in diameter centered approximately at α(J2000.0) = $02^h05^m37^s$, δ(J2000.0) = $+64^\circ49'50''$. This image is similar to one shown in Slane et al. (2004), which was also taken with the MDM 1.3 m telescope.

Greater detail in the remnant's Hα emission features can be seen in the higher resolution and somewhat deeper MDM 2.4 m telescope image shown in Figure 2. The extent of the remnant's emission structure covering this central region is readily visible in the 6510 Å continuum-subtracted version presented in Figure 3. Figures 2 and 3 show the remnant's emission to be resolved into diffuse knots and filaments on small spatial scales. There are also several faint, radially aligned streaks of emission roughly pointing to the middle of the remnant, especially numerous along the remnant's northeastern limb. These filaments give one the impression of a rapidly expanding nebulosity. (Note: The faint emission patch at the upper left portion of Fig. 3 is a data reduction artifact.)

A spherical distribution defines the bulk structure of the 3C 58's optical emission. That is, the majority of Hα emission features are located within a radius of 200″ centered on the remnant's pulsar PSR J0205+6449, with only a handful of faint Hα emission knots lying farther out along the northwestern and northeastern sections. These few outlying knots can be seen in Figure 4, which shows a continuum-subtracted version of the image shown in Figure 1. A circle of radius 200″, corresponding to 2.9 pc at a distance of 3 kpc is marked on this figure.

Striking differences between the remnant's largely circular optical emission structure as seen in Hα emission and its elliptical appearance in both the radio and X-rays are shown in Figure 5. In the top panel, we superimposed a 1.446 GHz VLA radio image taken on 1984 April 30 (L. Rudnick 1998, private communication) on our 1994 Hα image (Fig. 1). Ignoring the 10 yr time difference between observations, the remnant's radio emission can be seen to extend well past that of the optical in both the east and west directions, while the reverse is true toward the north and south. One also finds considerable optical emission in areas where there is little or no radio emission (e.g., along the north and south limbs) and also regions with extensive radio emission where the remnant's optical emission is virtually absent (e.g., the east and west limbs).

The remnant's optical emission and X-ray emission structures are also quite different. In the middle panel of Figure 5, we show a 2003 *Chandra* ACIS 0.5–10 keV image (Slane et al. 2004) overlaid again onto our 1994 Hα image. The remnant's X-ray emission can be seen to be largely confined to the remnant's optically bright central region. Although the X-ray image shows a complex of filamentary loops near the central pulsar (see Fig. 1 in Slane et al. 2004), there is only a weak correlation of these loops with optical features seen in Hα. That is to say, the remnant's central X-ray emission looplike structures are not coincident with optical knots and linear filaments. Finally, in the bottom panel of Figure 5 we show a mosaic of all three emission images overlaid.

Besides showing strong Hα and [N II] line emissions, many of the remnant's filaments and knots exhibit significant [O III] $\lambda\lambda$4959, 5007 line emission. However, the remnant's [O III] morphology is quite different from that seen in Hα. Figure 6 shows the structure of the remnant's [O III] brighter emission features (*upper panel*) alongside the remnant's Hα emission structure (*lower panel*) for comparison. As this figure shows, the majority of the strongly emitting [O III] features appear less clumpy compared to Hα emission and largely confined to the remnant's northwest quadrant. A long [O III] bright filament lies projected along the outer northwestern edge of the remnant and may mark the approximate location of the remnant's forward shock front in this region.

Relatively bright [O III] emission also extends farther west than that seen in Hα images and might extend even a bit farther to the west off the edge of the [O III] image shown. This may signal a greater number of filaments with higher shock velocities and/or

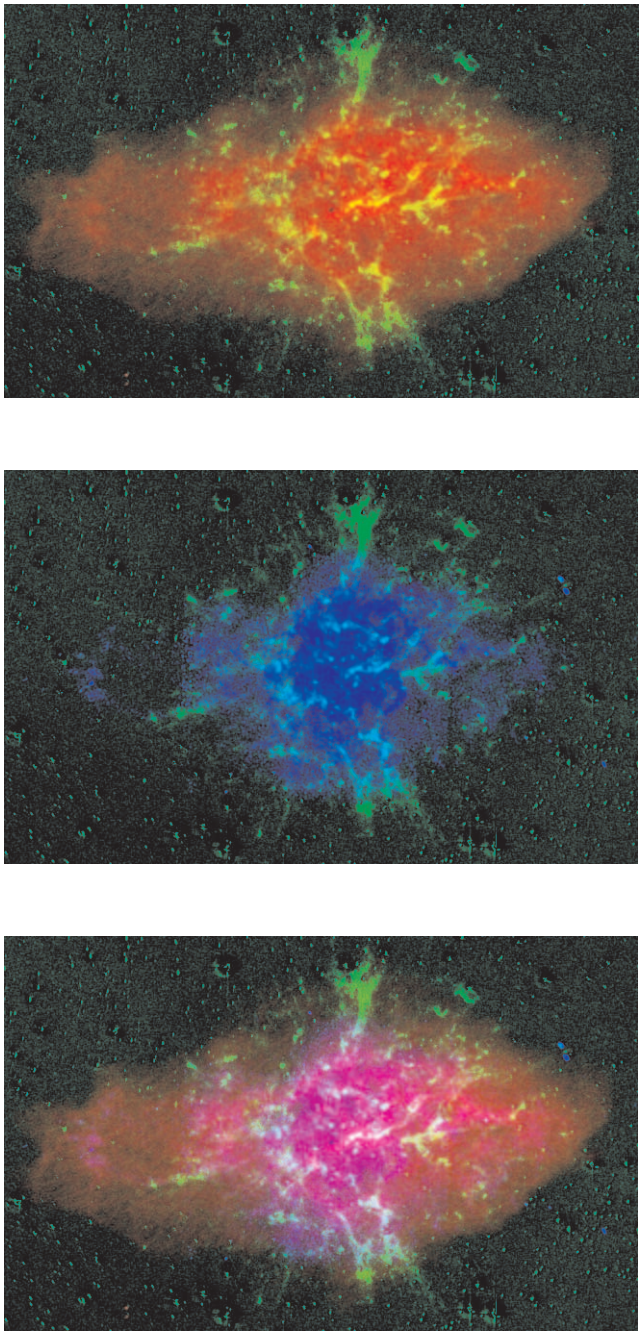

FIG. 5.—Comparison of 3C 58's optical Hα (*green*), 1.466 GHz radio (*red*), and 0.5–10 keV X-ray (*blue*) emissions.

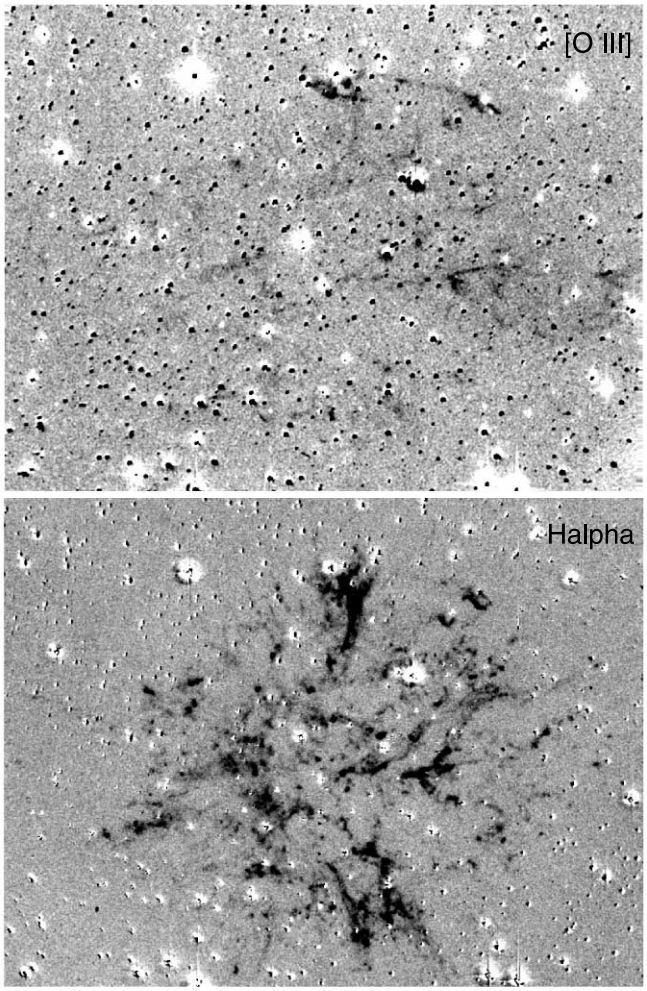

FIG. 6.—[O III] image (*top*) shown in comparison with an Hα image of 3C 58 (*bottom*).

closer knot proximity to the forward shock front along the remnant's western limb. Surprisingly, little or no [O III] emission is seen for many of the remnant's central and relatively bright Hα filaments and knots. This is in contrast to that seen along the western limb, where [O III] emission is present in areas with little or no detectable Hα emission.

3.1.1. *Filament Proper Motions*

Because previous studies reported finding surprisingly small proper motions for 3C 58's filaments assuming a connection with SN 1181, we examined images covering the largest time span available to investigate this issue. We compared a scanned copy of a 1977 Palomar 5 m red image of 3C 58 (van den Bergh 1978) to our 2005 October Hα image in order to estimate the proper motions for several knots and filaments around the periphery of the optical emission structure. Van den Bergh obtained an image of 3C 58 on 1977 October 9 using a 098-04 photographic emulsion and a Schott RG 645 filter, making the image primarily sensitive to both Hα and [N II] $\lambda\lambda$6548, 6583 line emissions. The time interval between images is 28.0 yr.

We investigated knot proper motions in five regions around the limb of the remnant with the regions indicated in Figure 7. Distortions in the scanned 1977 image, the relative weak detection of nebular features on this photograph, plus the inherent nonstellar appearance of most of the remnant's knots and filaments limited measurement accuracy of the derived proper motions. Nonetheless, the 28 yr time span between images was sufficiently large to provide useful estimates and relatively firm upper limits for the proper motions.

Figure 8 shows a relatively bright emission knot located along the remnant's northeastern limb (Knot 5Aa; $V_r = -550$ km s^{-1}). This knot exhibits a mushroom-like appearance with an extended emission tail giving the impression of high velocity. The measured shift of the emission knot between the two images is $1.25'' \pm 0.20''$, implying a proper motion of $0.035''$–$0.050''$ yr^{-1}. To place this motion in context with the proposed $\approx$827 yr remnant age, the knot's $155''$ displacement from the 3C 58 pulsar would require an average undecelerated proper motion of $0.19''$ yr^{-1}. This proper motion translates into a shift of $5.2''$ over 28 yr—or about the length of the scale bar shown in the 2005 image. Such a shift is

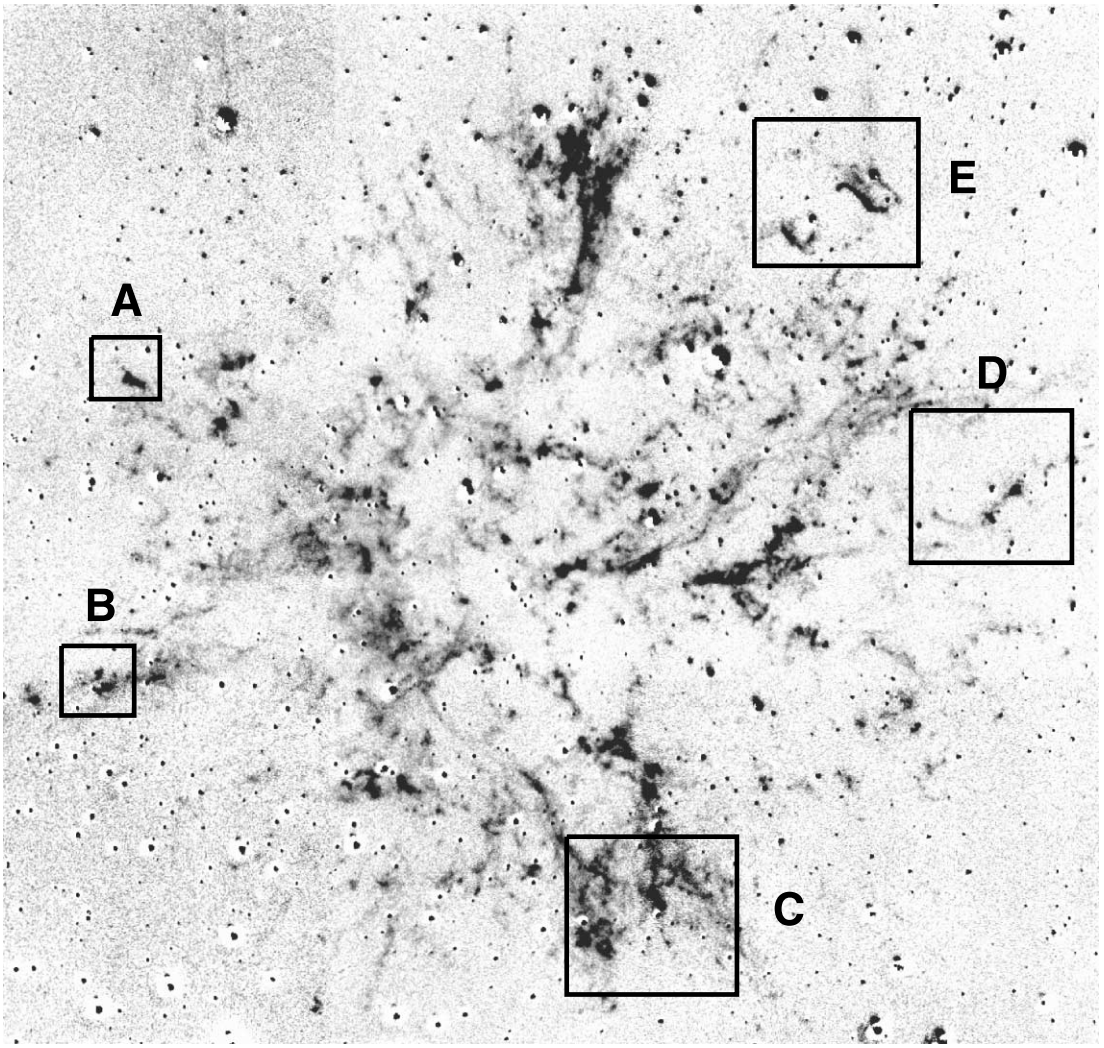

FIG. 7.—Continuum-subtracted Hα image with the five regions (A–E) examined for knot proper motions shown.

clearly not present notwithstanding possible scale distortions in the scanned 1977 image.

In general, we found that proper motions of 3C 58's emission features are typically small and often hard to visually perceive in images taken even one or two decades apart. However, in Figure 9 we show a region where knot proper motions are more apparent. The shift of the fainter northern knot appears to be relatively large at around 2″, implying a proper motion $\sim$0.07″ yr^{-1}. The displacement of the bright southern emission knot between the two images is much smaller, around 1.2″ $\pm$ 0.25″, implying a proper motion of 0.04″ $\pm$ 0.01″ yr^{-1}.

Figures 10, 11, and 12 show three other regions (Regions C–E on Fig. 7), all on the western side of the remnant. The observed positional shifts over the 28 yr image time span were found to be less than 2″ in all five regions. The thin filaments shown in Figure 12 are particularly interesting in that they are known to exhibit low radial velocities ($\leq$100 km s^{-1}; Kirshner & Fesen 1978). Consequently, their expansion should be primarily in the plane of the sky. However, the estimated shift of these filaments between the two images is just 0.6″ $\pm$ 0.15″, implying a proper motion of just 0.020″ $\pm$ 0.005″ yr^{-1}.

Measurements of these and a handful of other outlying emission knots and filaments yield 28 yr positional shifts of between 0.5″ and 2.0″, suggesting proper motions of 0.02″–0.07″ yr^{-1}. These values are in good agreement with previous proper motion estimates for the remnant's optical emission features (Fesen et al. 1988; van den Bergh 1990).

3.1.2. *Optical Emission near PSR J0205+6449*

Our Hα image covering the position of the remnant's 66 ms X-ray and radio pulsar (Murray et al. 2002; Camilo et al. 2002) is shown in Figure 13. We find no stellar source or Hα feature(s)

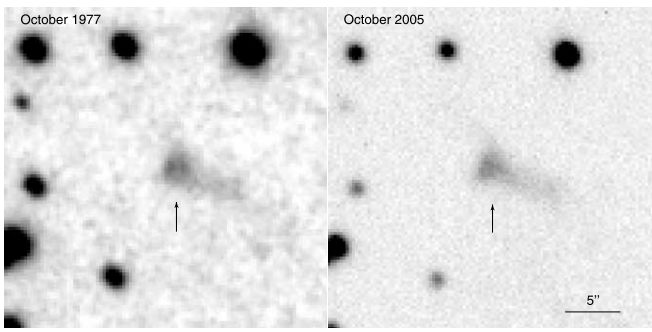

FIG. 8.—Proper-motion region A. Comparison of the position of Knot 5Aa located near the NE limb of 3C 58 (radial distance 155″) as seen in van den Bergh's 1977 photograph (*left*) and a 2005 Hα image (*right*). Shift of the emission knot between the two images is 1.25″ $\pm$ 0.20″, suggesting a proper motion of 0.035″–0.050″ yr^{-1}.

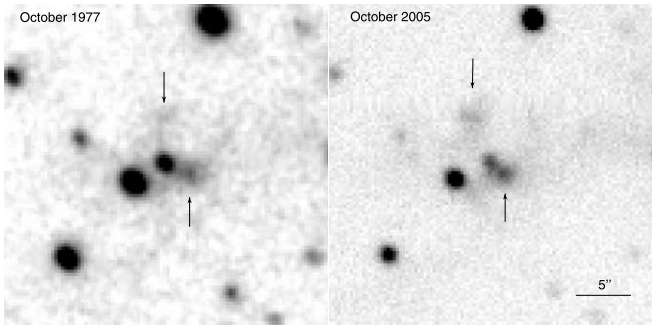

FIG. 9.—Proper-motion region B. Comparison of the position of two emission knots located some 15″ west of Knot 5Ag near the SE limb of 3C 58 (radial distance 156″) as seen in van den Bergh's 1977 photograph (*left*) and a 2005 Hα image (*right*). Shift of the brighter southern emission knot between the two images is $1.2'' \pm 0.25''$, suggesting a proper motion of $0.04'' \pm 0.01''$ yr^{-1}. Shift of the fainter northern knot appears larger at around 2″ suggests a proper motion $\sim 0.07''$ yr^{-1}.

near the pulsar's location. Specifically, we find no optical counterpart to the pulsar down to $m_R \sim 22.5$ based on comparisons of magnitudes for neighboring field stars using the USNO-A2.0 catalog (Monet et al. 1998).

A nondetection at this magnitude limit is not surprising since a pulsar's optical luminosity appears related to its spin-down rate, $\dot{P}$ (Goldoni et al. 1995). Although J0205+6449 has a relatively high $\dot{E}$ at 2.6×10^{37} ergs s^{-1} (Murray et al. 2002), the observed $\dot{P}$ of 1.93×10^{13} s s^{-1} places it between the Crab and Vela in its likely optical emission efficiency ($\eta_{\rm opt} = L_{\rm opt}/\dot{P}P$), suggesting a J0205+6449 might have $m_V = 25$ mag depending somewhat on the beaming factor. Alternatively, if we assume this pulsar has a X-ray/optical luminosity similar to optically observed pulsars then its $m_R \simeq 27$.

3.2. *Spectra*

Low-resolution spectra for 463 distinct emission regions in the 3C 58 remnant were extracted from our long-slit data. The locations of these regions are shown in Figure 14 overlaid onto a continuum-subtracted Hα image. Coordinate positions, relative x, y, and r offset distances from PSR J0205+6449, measured radial velocities, observed Hα fluxes, and relative line strengths were tabulated (see Table 2).

The relatively short exposures of our spectral survey combined with intrinsically weak hydrogen line emission lead to Hβ line emission being either weakly detected or not detected at all above the background for most knots. In a few of the brightest knots

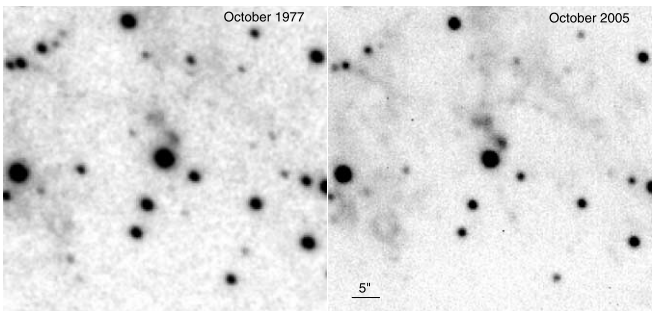

FIG. 10.—Proper-motion region C. Comparison of the position of Knot 7Bl located near the SW limb of 3C 58 (radial distance 132″) as seen in van den Bergh's 1977 photograph (*left*) and a 2005 Hα image (*right*). Shift of the emission knot between the two images is $1.15'' \pm 0.25''$, suggesting a proper motion of $0.035''$–$0.050''$ yr^{-1}.

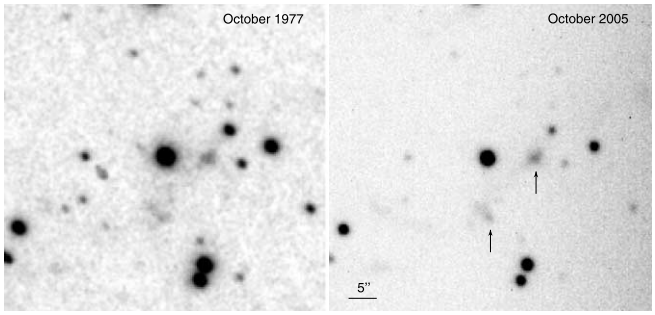

FIG. 11.—Proper-motion region D. Comparison of the position of two outlying knots near the western limb of 3C 58 (radial distances of 173″ and 165″) as seen in van den Bergh's 1977 photograph (*left*) and a 2005 Hα image (*right*). Shift of both emission knots between the two images is $\leq 1.5''$, suggesting a proper motion of $\leq 0.06''$ yr^{-1}.

(e.g., Knots 6Ib and 5Hb), however, Hβ was seen and could be measured yielding observed Hα/Hβ ratios between 5.7 and 6.5. Assuming an intrinsic ratio of 3.0, the three brightest knots showed ratios, implying $E(B-V) = 0.5$–0.7 ($A_V = 1.6$–2.3). This result is consistent with an earlier estimate of $E(B-V) \approx 0.7$ using better S/N spectral data on a only slightly larger sample of 3C 58 emission knots Fesen et al. (1988).

Six representative knot spectra are shown in Figure 15. The two spectra shown in the top panels illustrate filaments showing stronger Hα emission than [N II] λ6583 emission. These two examples are also instances where [S II] λ6716/λ6731 line ratios are $\approx$1.0, indicating electron densities around 400–500 cm^{-3}. The spectrum shown in the middle left plot is of a filament with strong [O III] emission. Conversely, the middle right plot shows a knot nearly absent in [O III] emission. Finally, the bottom two spectra show filaments that exhibit unusually strong [N II] emission, specifically, [N II] (λ6583 + λ6548)/H$\alpha \geq 8$.

3.2.1. *Knot Radial Velocities*

Measured radial velocities for the 463 knots range from -1070 to $+1100$ km s^{-1}. The average of the 62 fastest knots located within 75″ of the pulsar is 770 ± 155 km s^{-1}. This velocity range is similar to that reported from smaller studies of 3C 58's knots and filaments (e.g., the 50 knots in the study of Fesen et al. 1988).

In Figure 16, we plot observed knot velocities versus radial distance from the remnant's central pulsar. Two distinct kinematic populations of emission knots are seen: a shell with a peak expansion velocity of 1100 ± 75 km s^{-1} and a spread in velocity around ± 150 km s^{-1}, and a much more slowly expanding

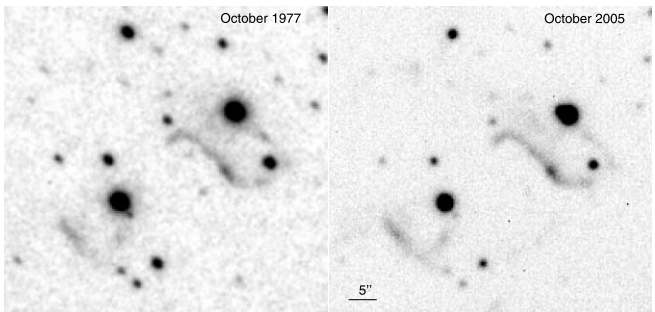

FIG. 12.—Proper-motion region E. Comparison of the position of outlying emission filaments and knots (5Ga,b and 5Ha,b: *center right*; 5Fa and 7Da: *lower left*) along the northwestern western limb of 3C 58 (radial distances of 175″–189″ and 147″, respectively) as seen in van den Bergh's 1977 photograph (*left*) and a 2005 Hα image (*right*). Shift of emission filaments between the two images is $0.6'' \pm 0.15''$, suggesting a proper motion of $0.020'' \pm 0.005''$ yr^{-1}.

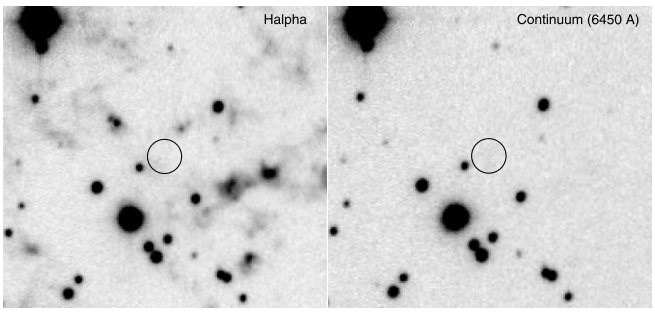

FIG. 13.—Region around the 3C 58's central pulsar, PSR J0205+6449, as seen in Hα emission (*left*) and red continuum at 6450 Å (*right*). Circles are 3″ in radius.

population of emission knots with $|v| \leq 300$ km s^{-1}. Toward the remnant center, one sees a clear separation in expansion velocity between the two populations with the two knot groups merging at radial distances around 100″. The remnant's optical emission appears to be fairly evenly divided between the two knot populations (fast and slow). For example, near the center of the remnant ($r \leq 75''$), where one sees the highest radial velocities, about half of emission features show low velocities ($|v| \leq 300$ km s^{-1}).

Attempts to model the observed velocity envelope using purely spherical expansion models failed to give good fits to the data due in part to considerable knot population identification confusion at large radial distances. For example, the curve shown in Figure 16 represents a spherical expansion with a peak velocity of 1050 km s^{-1} and a 150″ radius. While providing a fair match to the highest velocity knots near the center of the remnant (considering the ± 75 km s^{-1} radial velocity measurement error), this fit fails to encompass any of the remnant's emission beyond a radial distance of 150″ from the pulsar.

A secondary difficulty in modeling the remnant's expansion is uncertainty in the precise expansion center of 3C 58. We have used the pulsar's current position as the nominal remnant center in Figure 16 and all subsequent plots. However, as seen in the Crab, the pulsar could have experienced a significant kick of several hundred km s^{-1}, thereby moving it away from the SN explosion point. Unfortunately, proper motion measurements of the optical filaments and knots are too small (see above) to yield a definite expansion center as has been done on the Crab Nebula and Cassiopeia A.

A more serious problem fitting the observed radial velocity distribution with spherical expansion models is the apparent presence of a dipole expansion structure for 3C 58's high-velocity knot population. The projected spatial distributions of both high- and low-velocity emission populations of knots are presented in Figures 17, 18, 19, and 20. The size of the circles and squares in these plots is proportional to the absolute magnitude of a knot's measured radial velocity.

Evidence for a bipolar NE–SW bipolar expansion pattern can be clearly seen in Figure 17, where we plot high-velocity knots i.e., $|V_r| \geq 500$ km s^{-1}. For high-velocity knots lying within 90″

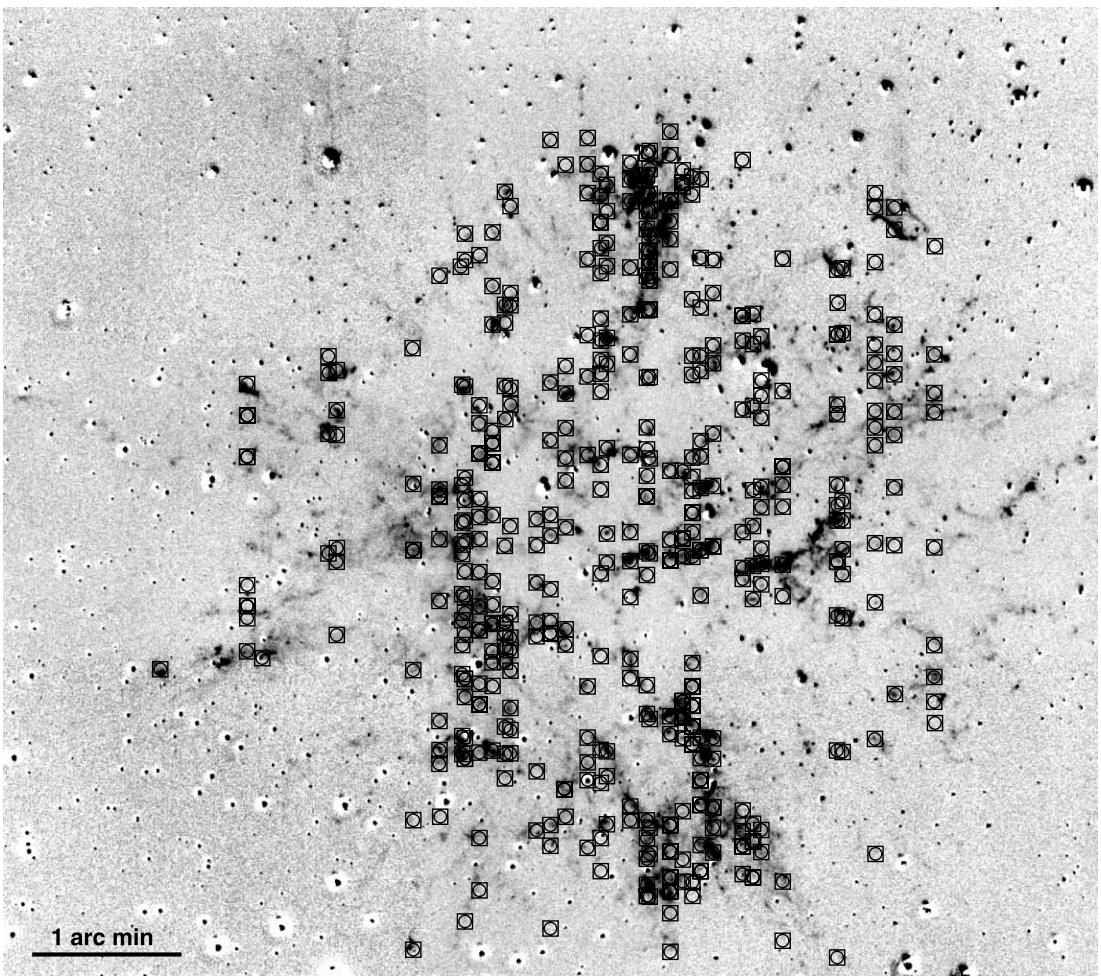

FIG. 14.—Continuum-subtracted Hα image of 3C 58 showing locations of the emission regions in the remnant for which low-dispersion optical spectra were extracted.

TABLE 2
OBSERVED EMISSION KNOTS IN 3C 58

Knot ID	α (J2000.0)	δ (J2000.0)	x (arcsec)	y (arcsec)	R^a (arcsec)	V_r (km s^{-1})	F(Hα) (ergs cm^{-2} s^{-1})	[N II]/Hα	λ6716/λ6731	λ6300/Hα	[S II]/Hα	λ5007/Hα
4Aa.....	2 05 44.62	64 51 47.4	−42.8	125.4	132.5	130	2.0E−16	2.6	...	...	...	...
4Ab.....	2 05 44.63	64 51 26.0	−42.9	103.4	103.6	−590	4.0E−16	2.0	1.1	...	0.8	...
4Ac.....	2 05 44.64	64 51 10.6	−42.9	88.0	97.9	−700	1.3E−15	4.2	1.2	1.4	1.9	0.2
4Ad.....	2 05 44.66	64 50 28.2	−43.1	45.6	62.7	730	1.9E−16	5.0	...	...	...	...
4Ae.....	2 05 44.66	64 50 23.3	−43.1	40.7	59.2	−90	3.2E−16	1.5	...	...	...	...
4Ae.....	2 05 44.66	64 50 23.3	−43.1	40.7	59.2	720	...	...	...	...	...	...
4Af.....	2 05 44.66	64 50 15.5	−43.1	33.0	54.3	120	3.0E−16	2.7	...	...	...	...
4Af.....	2 05 44.66	64 50 15.5	−43.1	33.0	54.3	570	...	...	...	...	...	...
4Ag.....	2 05 44.67	64 49 54.6	−43.2	12.1	44.8	0	6.2E−16	2.2	...	...	...	...
4Ah.....	2 05 44.68	64 49 28.2	−43.2	−14.3	45.5	120	6.1E−16	2.1	...	...	0.6	...
4Ai.....	2 05 44.69	64 49 18.9	−43.3	−23.7	49.6	70	8.1E−16	2.1	0.8	...	0.9	...
4Aj.....	2 05 44.69	64 49 11.2	−43.3	−31.9	53.5	550	8.6E−16	3.6	...	0.7	...	1.8
4Aj.....	2 05 44.69	64 49 11.2	−43.3	−31.9	53.5	50	...	...	...	...	...	...
4Ak.....	2 05 44.70	64 49 00.2	−43.3	−42.9	61.0	−1010	2.0E−16	5.7	1.1	...	2.1	...
4Al.....	2 05 44.70	64 48 55.8	−43.3	−47.3	63.8	−740	2.9E−16	4.2	...	...	...	...
4Am.....	2 05 44.70	64 48 46.4	−43.4	−56.7	71.4	−840	1.3E−17	11	...	...	...	...
4An.....	2 05 44.71	64 48 20.6	−43.4	−82.5	93.3	−140	1.6E−15	2.9	...	...	...	...
4Ba.....	2 05 43.48	64 51 57.9	−35.6	135.3	139.9	−10	3.7E−16	2.0	...	...	...	...
4Bb.....	2 05 43.50	64 51 23.2	−35.7	100.7	106.8	−660	4.8E−16	2.5	...	...	...	...
4Bc.....	2 05 43.50	64 51 18.3	−35.7	95.7	102.1	−670	7.1E−16	3.1	1.0	...	1.0	...
4Bd.....	2 05 43.52	64 50 45.3	−35.8	62.7	72.2	−70	1.6E−16	2.9	...	...	...	...
4Be.....	2 05 43.52	64 50 38.7	−35.8	56.1	66.6	−120	6.0E−16	2.2	0.8	...	0.9	...
4Bf.....	2 05 43.55	64 49 50.2	−36.0	7.1	36.7	50	4.6E−16	2.5	...	...	...	...
4Bg.....	2 05 43.56	64 49 15.0	−36.1	−27.5	45.4	590	9.0E−17	5.4	...	...	...	...
4Bh.....	2 05 43.57	64 49 05.7	−36.1	−36.9	51.6	−1070	6.0E−16	3.1	1.4	...	1.6	...
4Bi.....	2 05 43.57	64 49 00.7	−36.1	−42.4	55.7	−660	2.0E−16	7.5	...	...	...	...
4Bj.....	2 05 43.57	64 48 52.5	−36.2	−50.6	62.2	−760	4.3E−16	4.3	1.4	...	...	...
4Bk.....	2 05 43.58	64 48 37.6	−36.2	−65.5	74.8	−120	5.0E−16	4.1	...	...	...	...
4Bl.....	2 05 43.58	64 48 28.8	−36.2	−74.3	82.6	−120	2.9E−16	3.0	...	...	...	...
4Bm.....	2 05 43.59	64 48 19.5	−36.4	−82.9	90.6	−40	...	...	...	...	...	...

NOTES.—Units of right ascension are hours, minutes, and seconds, and units of declination are degrees, arcminutes, and arcseconds. Table 2 is available in its entirety in the electronic edition of the *Astrophysical Journal Supplement*. A portion is shown here for guidance regarding its form and content.

of the pulsar's current location (i.e., $\Delta\alpha = 0''$, $\Delta\delta = 0''$) one can see a strong symmetry with blueshifted (*circles*) and redshifted (*squares*) located preferentially north and south of the pulsar. Moreover, the highest velocity knots (i.e., larger symbol sizes) are seen to be tightly clustered in a band across the remnant center, starting in the northwest with positive velocities (squares) and ending in the southeast with high negative velocities (circles). Rather than observing the highest velocities closest to the pulsar or nominal remnant center, one finds knot radial velocities increasing along this central NW–SE band with increasing distance away from the pulsar.

However, this bipolar symmetry seen close to the pulsar is broken at larger radial distances (Fig. 17, *right panel*). While only a handful of redshifted knots are seen to lie in the predominately blueshifted southern emission regions, a fair number of blueshifted knots are seen in the remnant's outer northern filaments. The locations of all high-velocity knots projected on the continuum-subtracted Hα image are shown in Figure 18. As in Figure 17, knots with positive or negative velocities are shown color-coded. The central NW–SE band of optical emission knots can be seen running across the remnant's central region with knot velocities switching from positive (*red*) to negative (*blue*) velocities just south of the pulsar's position.

In sharp contrast to the projected distribution of high-velocity knots, the spatial distribution of the remnant's low-velocity knots, i.e., $|V| < 400$ km s^{-1}, appears more uniform (Figs. 19 and 20). The tendency for higher velocity emission knots seen here (both positive and negative) to appear more numerous near the remnant edges is likely due the detection of some high-velocity knots entering this low-velocity knot sample with increasing radial distance where an increasing fraction of their expansion velocity lies in the plane of the sky. We note that our slit coverage of the remnant was less complete along the eastern and western limbs. This led to an apparent lack of positive low-velocity knots along the east and west limbs may not reflect a real absence of positive, low-velocity emission features.

3.2.2. *Emission Line Ratios*

Measured [S II]/Hα ratios for all knots (within measurement uncertainties) lie above the well established value of 0.4 for shock heated gas (Raymond 1979; Fesen et al. 1985; Blair & Long 1997). The relatively strong [O I] $\lambda\lambda$6300, 6364 emission seen in many of these knots is additional evidence for shocks since [O I] line emission is weak relative to that of Hα in H II regions and photoionized nebulae (Fesen et al. 1985).

Strong [N II] $\lambda\lambda$6548, 6583 emission relative to Hα appears quite common in 3C 58 filaments, with many knots showing [N II]/H$\alpha \sim 3$–10. The bottom two spectra shown in Figure 15 are examples of knots that exhibit unusually strong [N II] emission. The fact that [S II]/Hα ratios in these knots are not unusually high suggests that large (λ6583 + λ6548)/Hα ratios seen in these knots are due to relatively strong [N II] and not weak Hα emission.

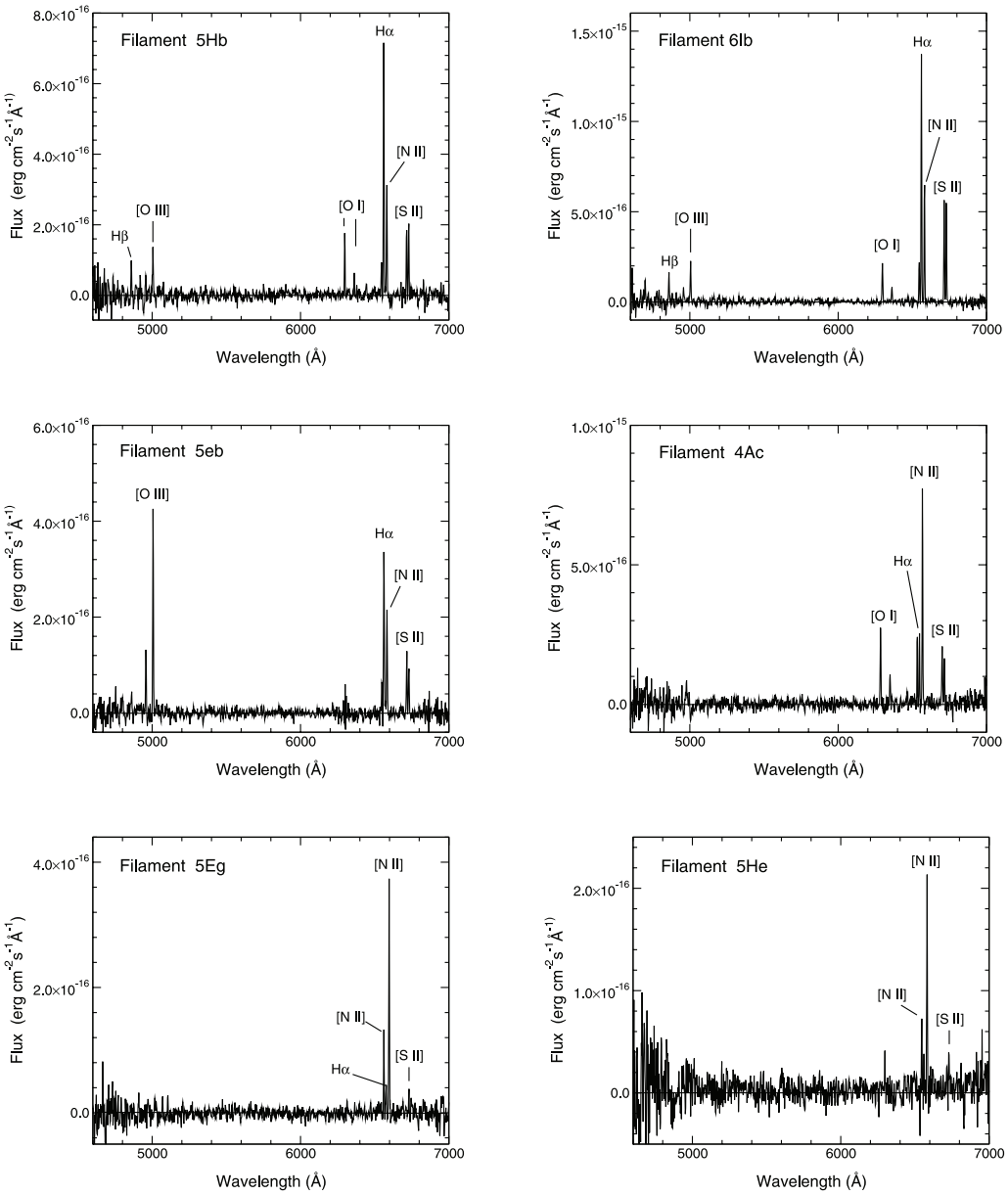

FIG. 15.—Spectra of six representative 3C 58 filaments.

Variations in knot [N II]/Hα ratios do not show a clear spatial pattern across the remnant. This is shown seen in Figures 21 and 22, where we plot the locations of all knots divided into two groups based on [N II]/Hα ratios above and below 3.

However, a strong correlation of knot [N II]/Hα ratios with radial velocities can be seen in Figure 23, where we plot knot radial velocities as a function of radial distance from the central pulsar. Unlike Figure 16, here knots are plotted with the symbol size indicating measured [N II]/Hα ratios. From this figure, one can readily see that, especially at radial distances less than 100″, the population of high-velocity knots exhibit on average much stronger [N II] emission compared to lower velocity knots. Due to projection effects, the two populations begin to merge toward the remnant's limb, i.e., at a radial distances from the pulsar greater than 120″. While the population of high-velocity knots exhibit [N II]/Hα values ranging from 1 to 10, no low-velocity knots exhibit values above $\simeq$7. Thus, the two knot populations differ not only in expansion velocity but also in chemical composition.

We also investigated whether there was a significant difference in knot density between the two knot populations. Generally, we found the density sensitive [S II] λ6716/λ6731 line ratio, where accurately measured, was often between the low-density limit of 1.4 and 1.0. If we assume a shock velocity of $\simeq$100 km s^{-1} suggested by the strength of [O III] $\lambda\lambda$4959, 5007 line emission, then using the formula given in Fesen & Kirshner (1980) the observed 6716.6731 ratio suggests electron densities of 100–500 cm^{-3} imply preshock densities of 2–10 cm^{-3}. However, this line flux strength ratio did reach values as small as 0.7–0.5 in a few cases (see Table 2) indicating much higher postshock densities of 3000–10,000 cm^{-1}.

The distribution of knot density with radial velocity is shown in Figure 24. To lessen the effect of measurement accuracy of this

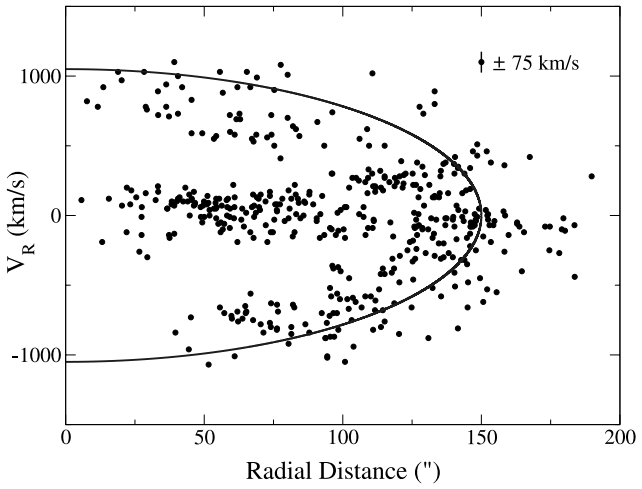

FIG. 16.—Plot of observed radial velocity with projected radial distance from the central X-ray point source (PSR J0205+6449). The curve shown indicates a 1050 km s^{-1} spherically expanding remnant 150″ in radius.

ratio from the fainter emission knots, this plot shows the [S II] ratio only for the brighter 3C 58 knots, i.e., having Hα flux $\geq 1 \times 10^{-15}$ ergs cm^{-2} s^{-1}. Symbol size is proportional to the measured [S II] 6716/6731 line ratio, and thus the smaller symbol size indicates higher knot electron density. The figure reveals no obvious correlation of knot density with expansion velocity.

4. DISCUSSION

4.1. *Optical Morphology of 3C 58*

The image and spectral data presented above reveal a more extensive and organized optical structure for 3C 58 than previously realized, but one that is surprisingly similar in several aspects to that of the Crab Nebula. The total ensemble of emission features in the remnant is complex on small scales, with bright knots often embedded in a fainter and more diffuse structure. We estimate that there may be as many as a 1000 individual Hα+[N II] emission knots or diffuse patches in the 3C 58 remnant. Our spectra of over 450 knots, therefore, may have sampled only about half of the remnant's optical structure.

In Hα emission, 3C 58 is more circular in shape than that seen in either radio or X-rays (Fig. 5). Although different in gross structure, there are a few small regions that do appear spatially correlated in the radio and optical. One is a line of optical knots in the southeast that exactly matches the location of a sharp change in radio flux. However, in general one finds the majority of optical knots have little if any counterpart features in the radio. This is also true for the optical versus X-rays, as already noted by Slane et al. (2002).

4.2. *Evidence for Circumstellar Material and an Asymmetrical SN Explosion*

The striking bimodal distribution of expansion velocities within the remnant (Fig. 16) shows the remnant clearly possesses two knot populations: a high-velocity expansion knot population with $|\bar{v}| = 770 \pm 155$ km s^{-1} and one low-velocity population ($|v| \leq 300$ km s^{-1}). The simplest interpretation for the presence of these two populations of emission knots is that the higher velocity group represents SN ejecta, while the slower one represents shocked circumstellar material (CSM). In this scenario, the low-velocity knots are shocked, pre-SN mass loss material originally ejected with a velocity of at most a few hundred km s^{-1}. This material makes up a significant component of the remnant's optical structure. Indeed, nearly half of the observed optical emission near the remnant center is expanding with a velocity less than 250 km s^{-1}. Radio 21 cm observations suggest this circumstellar material is unlikely to be spatially extensive (Wallace et al. 1994).

The remnant's higher velocity knots ($|v| \geq 500$ km s^{-1}), presumably SN ejecta, lie within a thick shell-like structure (Fig. 16). The distribution of this ejecta shows strong evidence for a NE–SW bipolar expansion structure. This was probably not seen previous in earlier studies of 3C 58 due to incomplete coverage of the remnant's optical emission.

As shown in Figure 17, blue and redshifted ejecta knots are well segregated near the middle of the remnant. In Figure 25, we present a toy model of the remnant's bipolar expansion. The central NW–SE band of redshifted and blueshifted high-velocity knots seen running across the middle 3C 58 is suggestive of an expanding ejecta ring. In such a scenario, redshifted knots located some 10″–70″ W, NW, and SE of the pulsar (position 0, 0) represent receding (rear) portions of this ring. The group of SE redshifted knots nearly coincident (in projection) with about a dozen

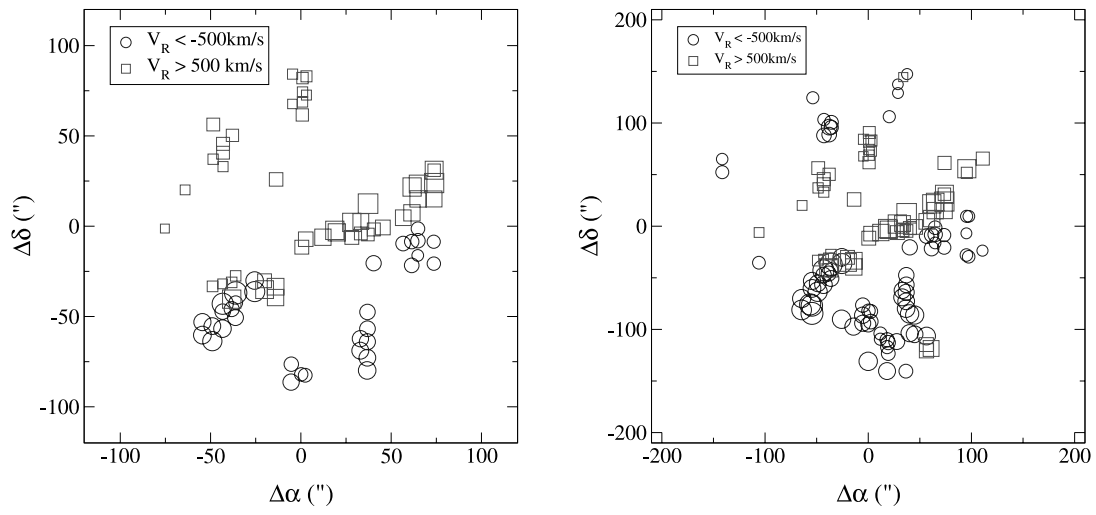

FIG. 17.—*Left*: Distribution plot of 3C 58's high-velocity emission knots ($|v| \geq 500$ km s^{-1}) with projected locations within 90″ of the pulsar, PSR J0205+6449. *Right*: Distribution plot for all 3C 58's high-velocity emission knots. [*See the electronic edition of the Supplement for a color version of this figure.*]

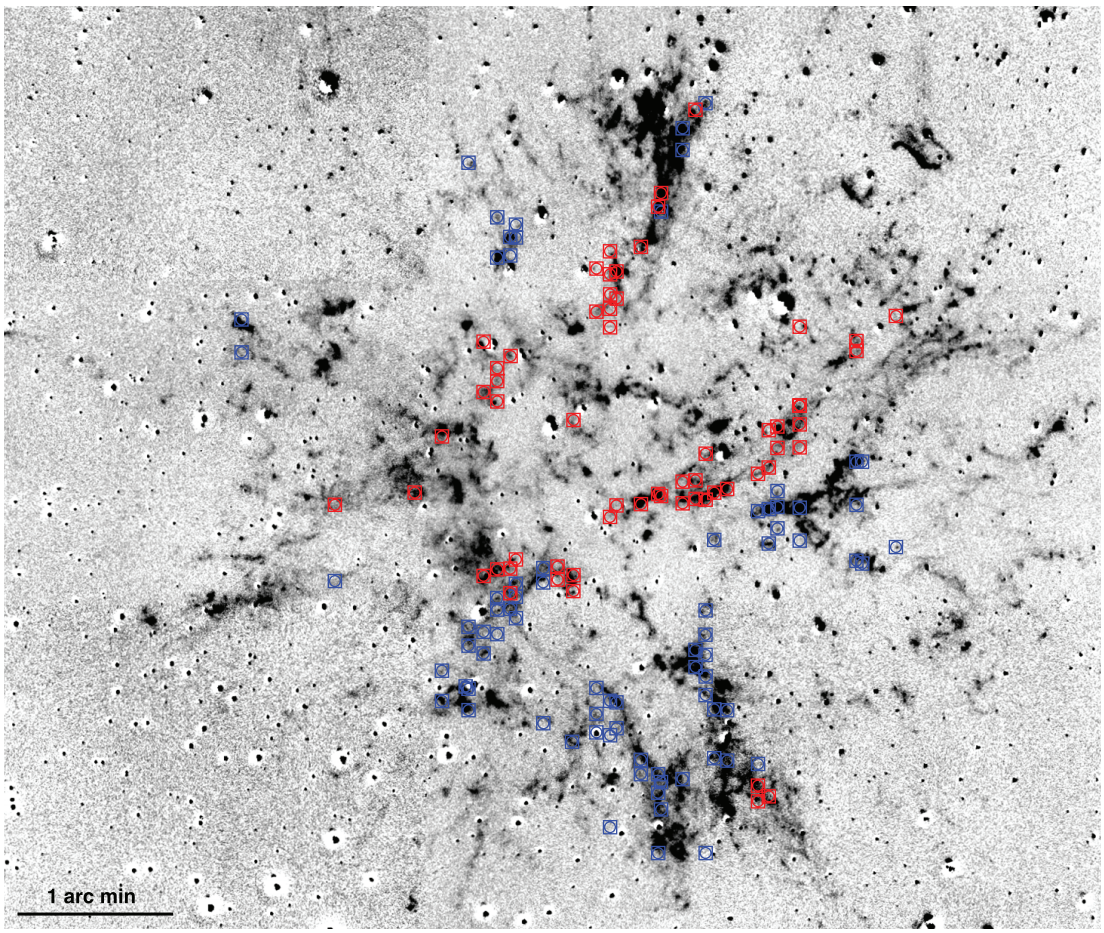

FIG. 18.—Distribution of all high-velocity emission knots (i.e., >500 km s^{-1}) overlaid onto continuum-subtracted Hα image. Measured positive and negative radial velocity values are color-coded red and blue, respectively.

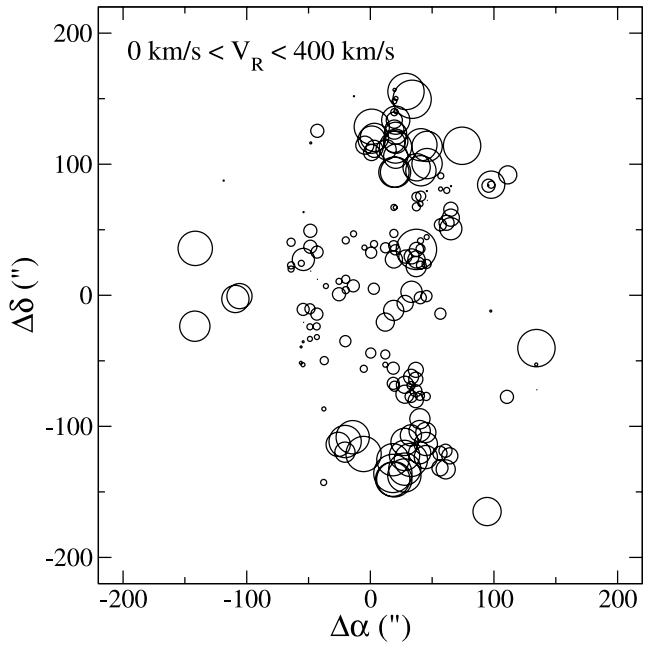

FIG. 19.—Distribution plot of 3C 58 knots showing low positive radial velocities (i.e., $V < 400$ km s^{-1}). Symbol size corresponds to the absolute magnitude of the radial velocity within this velocity range. The plot is centered on the position of the central pulsar, PSR J0205+6449.

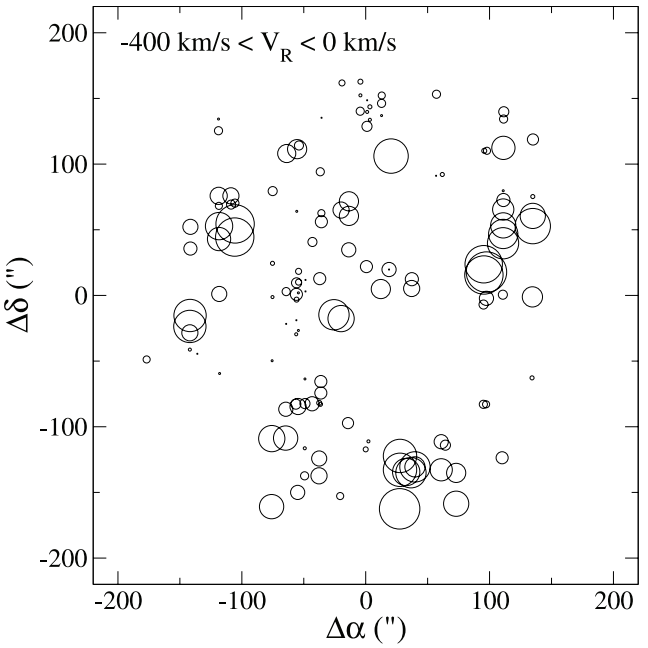

FIG. 20.—Distribution plot of 3C 58 knots showing low negative radial velocities (i.e., $V < 400$ km s^{-1}). Symbol size corresponds to the absolute magnitude of the radial velocity within this velocity. The plot is centered on the position of the central pulsar, PSR J0205+6449.

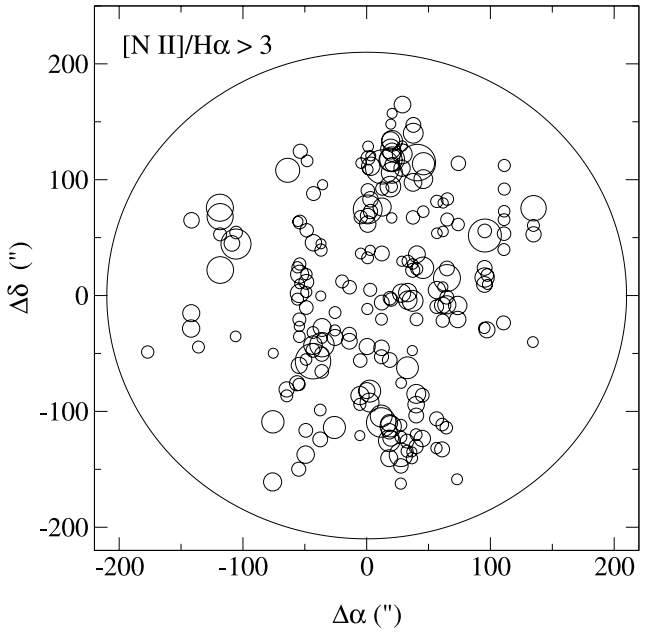

FIG. 21.—Plot of the distribution of knots showing [N II] λλ6583,6548/Hα line emission ratio greater than 3. Larger circle size reflects larger ratio value. The plot is centered on the position of the central pulsar, PSR J0205+6449.

highly blueshifted knots farther to the SE would lie behind these blueshifted knots, which are on the front and approaching side of the ring. Likewise, some of the western blueshifted knots positioned just below the ring shown in our toy model would also be located on the near side of this expanding ring. If correct, the ring is then either split toward the west or somewhat broader than depicted here. If this ring is centered on the remnant's true expansion center, then the displacement of the pulsar PSR J0205+6449 to the north of this ring might imply a significant proper motion.

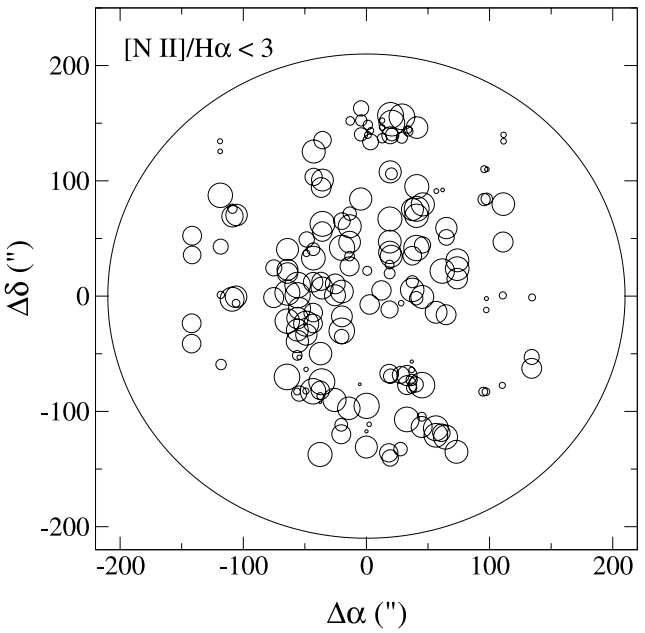

FIG. 22.—Plot of the distribution of knots showing [N II] λλ6583,6548/Hα line emission ratio less than 3. Larger circle size reflects larger ratio value. The plot is centered on the position of the central pulsar, PSR J0205+6449.

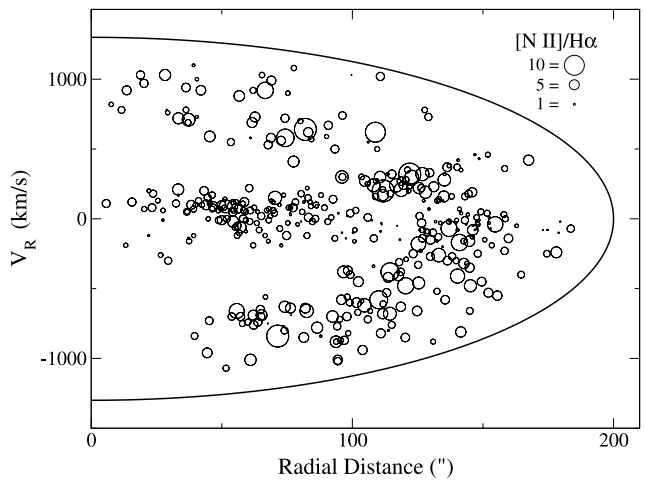

FIG. 23.—Distribution of the radial velocity of all emission knots in 3C 58 with respect to radial distance (from the pulsar PSR J0205+6449). The symbol size reflects the observed [N II] (λ6583+λ6548)/Hα line emission ratio. The curve represents a spherical expansion at 1300 km s^{-1} and a 200″ radius remnant.

Our expanding cone model can explain the presence of high radial velocity material at large radii, where normally one would expect the radial velocities to be small, due to projection effects. However, to match the observations, the expansion cone may be tilted substantially toward us, much more so than that depicted in Figure 25. In any case, our toy model is should be viewed as a first step in better understanding the expansion dynamics of this young SNR.

Based mainly on the NW–SE alignment of the central high-velocity filaments, the proposed expanding ring is tilted at a position angle of $33^\circ \pm 15^\circ$. The close projected coincidence of the blue and redshifted knots also means the ring is being viewed nearly edge-on. The fact that the remnant's highest velocity redshifted and blueshifted knots lie a significant distance away from the nominal remnant center means that the remnant's maximum expansion velocity exceeds the largest observed radial velocity value of 1100 km s^{-1}. Adopting a 3 kpc distance, a proper motion of 0.02″ yr^{-1} for the highest velocity knots (1100 km s^{-1})

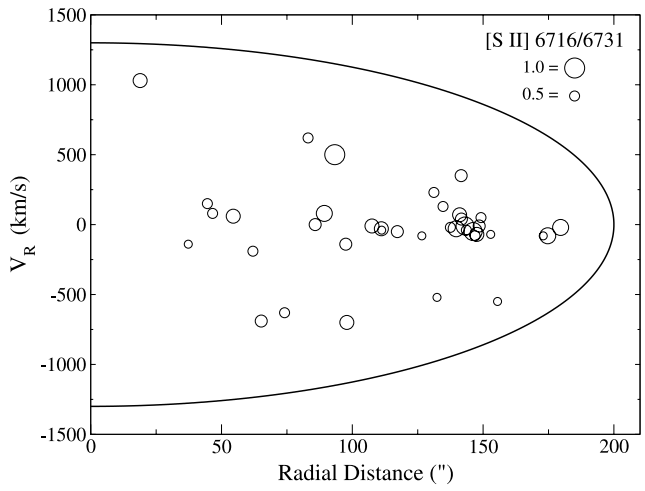

FIG. 24.—Radial velocity of knots in 3C 58 with Hα flux $\geq 1 \times 10^{-15}$ ergs cm^{-2} s^{-1}. Symbol size is proportional to the measured [S II] λλ6716/6731 line ratio; hence, the smaller symbol size indicates higher knot electron density. The curve represents a spherical expansion at 1300 km s^{-1}.

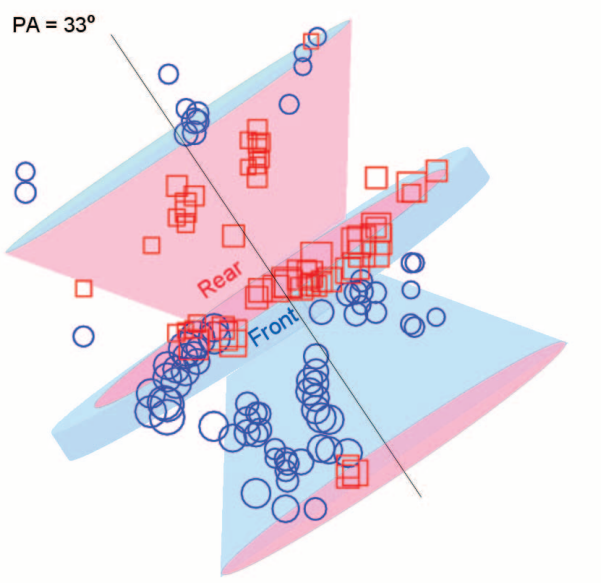

FIG. 25.—Proposed toy expansion model of 3C 58 consisting of a central ring of ejecta with northeast and southwest bipolar expansion ejecta cones. Model is superimposed on the distribution of 3C 58's high-velocity emission knots ($|v| \geq 500$ km s^{-1}; see Fig. 17) with size of the red squares and blue circles indicating the magnitude of the observed redshift or blueshifts, respectively.

located 30″–45″ displaced from the pulsar, we then estimate a maximum velocity of around 1150 km s^{-1}.

Outside of the central region, the distribution of the remnant's high-velocity knots appears asymmetric and probably bipolar. South of the central NW–SW line of knots, nearly all of high-velocity knots we observed appear blueshifted with most northern knots redshifted.

One interpretation of this situation are tilted and opposing expanding cones with the southern cone angled somewhat toward the observer, while the northern one is directed into the sky. This would make a majority of the ejecta located in the south and southwest appear blueshifted with the only high-velocity redshifted knots located on the rear, outlying edge of the cone where their projected velocities would exceed our high-velocity knot 500 km s^{-1} cutoff. The reverse would hold in the north and northeast sections where high-velocity knots are predominately redshifted. There, the expansion might be directed away from the observer into the plane of the sky with only knots along the outermost edges of this northern expansion exhibiting blueshifted high velocities.

A bipolar expansion for 3C 58 is new and was not be previously recognized due principally to a lack of spectra on a sufficient number of knots. It is interesting to note that a NE–SW expansion orientation is quite different from that seen in recent X-ray studies, which shows a N–S synchrotron torus around the central pulsar with E–W jets indicating an east–west orientation of the projected rotation axis of the pulsar Slane et al. (2004). While the nature of such expansion–pulsar misalignments is unclear, we note that a similar discord between pulsar generated synchrotron torus and rotation axis with expansion symmetries in SN ejecta is seen in the Crab Nebula (Fesen et al. 1997), the remnant probably most similar to 3C 58.

4.3. *3C 58 Knot Chemical Abundances*

The two kinematically distinct velocity populations in 3C 58 appear quite different chemically based on their average [N II]/Hα line ratios (Fig. 23). The strong [N II] emission ([N II]/H$\alpha \simeq$ 3–10) observed in the remnant cannot be explained by shocks using solar composition (Cox & Raymond 1985; Hartigan et al. 1994). Instead, it indicates high N/H abundances at least several times solar (MacAlpine et al. 1996; Zanin & Kerber 2000). Similarly, strong [N II] line emission is seen in stellar mass loss material processed by the CNO cycle like than seen in Wolf-Rayet nebulae (e.g., NGC 6888, Kwitter 1981) and in young SNRs (e.g., the QSFs in Cas A; van den Bergh 1971; Peimbert & van den Bergh 1971; Fesen 2001) including the Crab Nebula (Fesen & Kirshner 1982; MacAlpine et al. 1989; MacAlpine et al. 1996).

The relatively strong [N II] line strengths in 3C 58's low-velocity knots also suggests the presence of a substantial amount of N enrichment in this circumstellar material as well. The slower expanding knots likely represent mass loss material ejected by the progenitor not long before the 3C 58 supernova explosion, which was subsequently shocked by the expanding SNR and thus made optically visible. The fact that the remnant appears circular in the optical despite a strong NE–SW dipole asymmetry not only reflects the spherical propagation of the remnant's expanding shock front but also the distribution of this CS material.

The presence of surrounding shocked CSM may also account for the thermal X-ray component seen in the remnant's outermost regions (Slane et al. 2004). An interaction with surrounding CSM is also supported by recent models of the remnant's pulsar wind nebula (van der Swaluw 2003). Additional evidence for the remnant's interaction with fairly dense surrounding material comes from our [O III] image, which shows a long [O III] bright filament located at the outer edge of the remnant's Hα emission structure along the northwestern limb.

4.4. *Similarity of 3C 58 with the Crab Nebula*

In terms of optical and expansion properties, 3C 58 is fairly similar to that of the Crab Nebula. Both remnants exhibit a thick shell of ~800 to 1200 km s^{-1} velocity ejecta with strong [N II] line emission relative to Hα (Fesen & Kirshner 1982; MacAlpine et al. 1996).

Moreover, our survey of 3C 58's optical emission shows, much like that seen for the Crab Nebula, virtually no intermediate-velocity material. The usual explanation in the case of the Crab is that such ejecta have been swept up by the Crab's powerful pulsar wind nebula (PWN). But that process seems unlikely to have occurred in 3C 58 given its weak PWN (3×10^{37} ergs s^{-1}), some 20 times less than that of the Crab (Murray et al. 2002). This may suggest that the 3C 58 supernova simply did not eject much optically visible material with velocities between 300 and 600 km s^{-1}.

We also note that the Crab Nebula, like as we have found in 3C 58, may also contain considerable pre-SN circumstellar mass loss material. The evidence comes from the presence of dense filaments arranged in an E–W ring of He-rich filaments (MacAlpine et al. 1989; Lawrence et al. 1995; Fesen et al. 1997; Smith 2003). This He-rich band has been interpreted as being in part pre-SN mass loss material, which may have played a role in the formation of the Crab's prominent east and west synchrotron "bays" (Fesen et al. 1992, 1997). In the case of the Crab, it has been proposed that this ring of CSM may have led to a N–S bipolar expansion. While there is now evidence for a bipolar expansion in 3C 58, it is far less clear that it is a result of any surrounding pre-SN circumstellar material.

4.5. *Is 3C 58 the Remnant of SN 1181?*

One of the most puzzling aspects of 3C 58 is that many of its physical properties do not match those expected for a young remnant. That is, it is difficult to reconcile 3C 58's size, proper motions, expansion velocity, pulsar, and pulsar wind nebula properties with an age of 827 yr. Here we briefly discuss the likelihood that 3C 58

TABLE 3
AGE ESTIMATES FOR 3C 58

Property/Observation	Age (yr)	Reference
Historical 1181 guest star connection	827	Stephenson (1971); Stephenson & Green (2002)
Pulsar wind nebula evolution	~2400	Swaluw (2003), Chevalier (2004, 2005)
Pulsar wind nebula energy	~2500	Chevalier (2004, 2005)
Optical knot radial velocities	~3000	Fesen et al. (1988); this work
Optical knot proper motions	~3500	Fesen et al. (1988); van den Bergh (1990); this work
Pulsar location in thermal X-ray shell	~3700	Gotthelf et al. (2007)
Neutron star cooling models	≥5000	Slane et al. (2002)
Pulsar spin-down age	~5380	Murray et al. (2002)
Synchrotron expansion (radio)	~7000	Bietenholz (2006)

is the remnant of SN 1181 in light of results from our optical study together with other recent findings.

The historic records of the guest star sighted by Chinese and Japanese astronomers make it clear that a new, comparatively bright object was observed in the general vicinity of 3C 58 in 1181 August. It reached an estimated visual brightness around 0 mag and attracted considerable attention in China and Japan, and it may have even been sighted in Europe (Polcaro 2004).

In a series of papers, these Chinese and Japanese sightings have been interpreted by Stephenson and colleagues as being the supernova that resulted in the 3C 58 remnant (Stephenson 1971; Clark & Stephenson 1997; Stephenson & Green 1999; Stephenson & Green 2002). These authors claim that the association of 3C 58 with the guest star of 1181 can be made with a high degree of confidence. This conclusion is supported by the work of Liu (1983).

Huang (1986), however, questioned this 3C 58−1181 guest star connection. In an unpublished manuscript describing in more detail his arguments, Huang stated that (1) the 1181 SN was too faint ($M_V \approx -14$) to be associated with a remnant at a distance of ~3 kpc and a foreground extinction of 1.5 mag and (2) that Stephenson and Liu may have misidentified the ancient star asterism *Ch'uan-she*, which the Chinese records indicated was nearest the 1181 star. Huang instead suggests that the guest star of 1181 probably occurred within 1° of the 5.8 mag star HD 9030 [α(J2000.0) = $01^h30.8^m$, δ(J2000.0) = $+66°6'$]. He also suggested that, because the 1181 star was visible for only about 6 months, it may have been a slow nova and not a supernova at all. However, there is no known SNR around this star's position, no less a young one (Green 2004), and no obvious nova candidate (Downes et al. 2005).

It is difficult to assess the accuracy and even the original meaning of brief and fragmentary historical astronomical records. In the case of 3C 58, the claim of Stephenson and others that 3C 58 is the SNR of the 1181 guest star appears not unreasonable. However, interpreting the few reported sightings and descriptions is not without uncertainty. Below we examine the observational properties of the 3C 58 remnant for evidence to support its association to the 1181 guest star.

We begin with the knot proper motions and radial velocity data collected in our optical study of the remnant described above. The proper motions of the 3C 58 knots we examined range between 0.02″ and 0.07″ yr^{-1}. These values agree qualitatively with the two previous proper motion estimates made by Fesen et al. (1988) and van den Bergh (1990). If these proper motions reflect undecelerated knot motions over the remnant lifetime, we estimate 3C 58 is around 3000–4000 yr old.

We also found that the average of the measured radial velocities for 3C 58's high-velocity optical knots is about 770 km s^{-1}. Adopting this velocity and assuming a distance of 3.0 kpc again with no knot deceleration, the locations of the outer optical emission features ($r \sim 150''$–$200''$; 2.2–2.9 pc) suggest an age of between 2700 and 3500 yr. Considering the likelihood of at least some knot deceleration, these values are then upper limits. Interestingly, a velocity of 770 km s^{-1} gives a proper motion of 0.054″ yr^{-1}, close to that actually observed for many outlying knots.

Our optical data on 3C 58 does not indicate a ~800 yr age. It is possible that the remnant's faster knot component have experienced significant deceleration due to interaction with surrounding CSM knots and filaments. However, this would require a high CSM filling factor plus a fairly uniform deceleration factor to avoid producing a wider spread in the high-velocity knot population than is observed.

The conclusion that 3C 58 may be much older than 827 yr has been reached in several recent studies of the remnant (see Table 3). Expansion measurements of 3C 58's filamentary synchrotron nebula show an expansion rate of 0.014% ± 0.003% yr^{-1}, corresponding to a velocity of 630 ± 70 km s^{-1} (Bietenholz 2006). This in turn suggests an age of ~7000 yr with a 3 σ lower limit of 4300 yr.

The internal energy of the remnant's PWN appears too large for the current pulsar spin-down luminosity if only 827 yr old ($\dot{E}t < E_{\rm int}$; Chevalier 2004, 2005). To explain the observed energy, the pulsar would have had to significantly spun down, inconsistent with a ~800 yr age. The pulsar's spin-down age is 5380 (Murray et al. 2002), which again is much larger than if it were the result of a 1181 supernova.

The remnant's PWN is also too large to have expanded in just 800 yr into the debris from a normal SN. Its size requires a much lower than expected density than can be plausibly explained by SN models (Chevalier 2004, 2005). However, models of the 3C 58 PWN match that expected if it is interacting with interstellar or circumstellar material (van der Swaluw 2003). The estimated swept-up mass by the expanding PWN based on X-ray measurements is more than 30 times than that expected for an age of 827 yr (Chevalier 2004, 2005). Finally, the sharp, low-frequency spectral break seen in 3C 58 suggests an age older than 800 yr (Green & Scheuer 1992; Woltjer et al. 1997; Bietenholz 2006).

In summary, the majority of 3C 58 observations support the notion that 3C 58 is unconnected to the 1181 guest star. If this is correct, it then begs the question as to what is the true 1181 supernova remnant? Several authors have wrestled with this dilemma and some have suggested that a faint as yet undetected SNR may exist in the vicinity near 3C 58 (Chevalier 2005; Bietenholz 2006). Also, as noted by Huang, it is not absolutely certain that the 1181 star was indeed a supernova. Nonetheless, the weight of the evidence on 3C 58 currently in hand points to an age >825 yr.

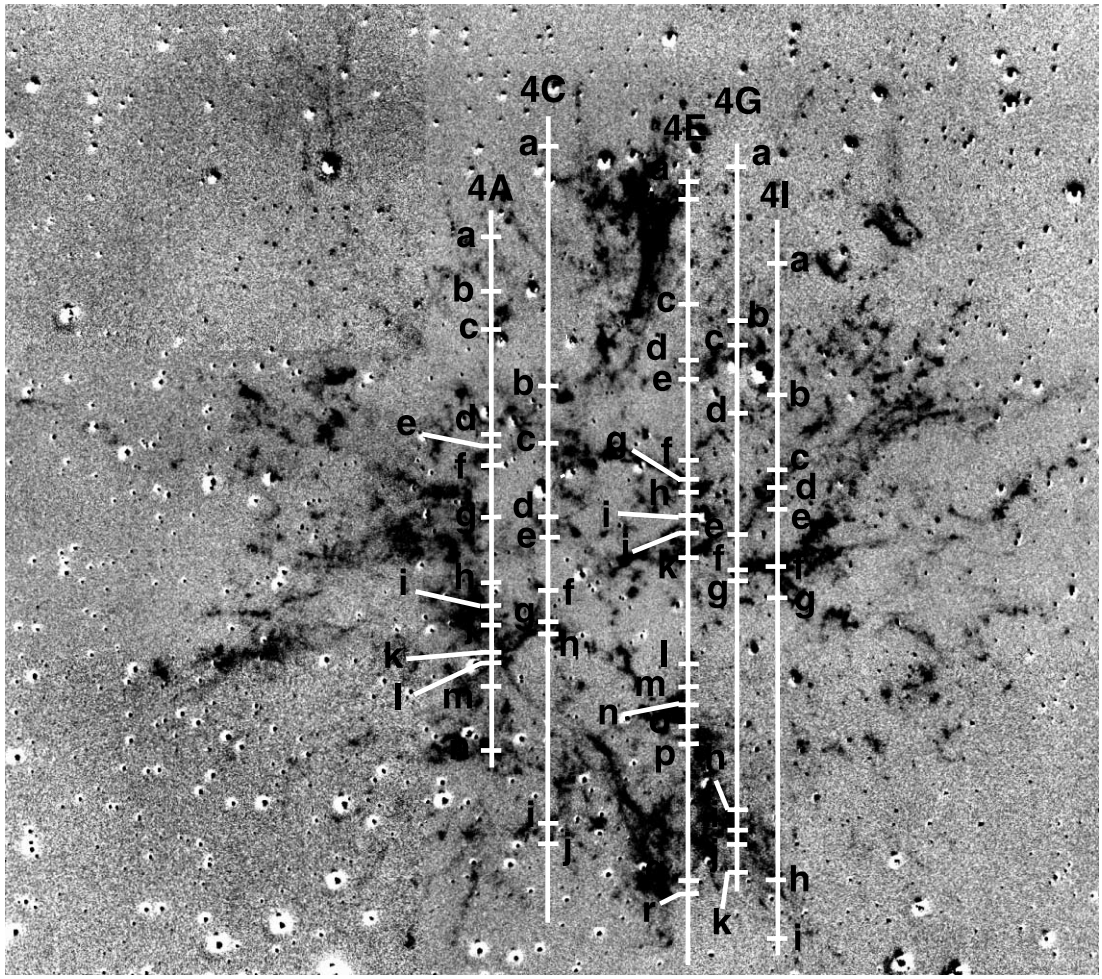

FIG. 26.—(*a*) Emission knot finding chart for slit positions 4A, 4C, 4E, 4G, and 4I. (*b*) Emission knot finding chart for slit positions 4B, 4D, 4F, and 4H. (*c*) Emission knot finding chart for slit positions 5A, 5C, 5E, 5G, and 5I. (*d*) Emission knot finding chart for slit positions 5B, 5D, 5F, and 5H. (*e*) Emission knot finding chart for slit positions 6A, 6D, 6G, and 6J. (*f*) Emission knot finding chart for slit positions 6B, 6E, 6H, and 6K. (*g*) Emission knot finding chart for slit positions 6C, 6F, 6I, and 6L. (*h*) Emission knot finding chart for slit positions 7A, 7C, and 7E. (*i*) Emission knot finding chart for slit positions 7B, 7D, and 7F. [*See the electronic edition of the Supplement for panels (b)–(i) of this figure.*]

Hence, both a renewed search for faint SNRs in this region of the sky and a reexamination of the 1181 historical records in light of recent observational findings may help resolve this puzzle.

5. CONCLUSIONS

We have presented results from a comprehensive imaging and spectroscopic survey o f the optical emission knots associated with the Galactic supernova remnant 3C 58. These data help better define the remnant's optical structure and kinematic properties. Our main findings are the following:

1. The remnant's emission consists of clumpy filaments and knots arranged in a complex structure covering an area roughly 400″ in diameter. We estimate that there may be as many as $\simeq$1000 individual Hα+[N II] emission knots or diffuse patches in the remnant.

2. 3C 58's Hα morphology is nearly circular and strikingly different from that seen in the radio. The remnant's [O III] emission structure is also quite different from that seen in Hα with a majority of strongly emitting [O III] features seen in the remnant's northwest quadrant.

3. We find no stellar optical counterpart to the pulsar, PSR J0205+6449, down to $m_R \sim 22.5$.

4. Proper motion estimates for several outlying emission knots using images spanning a 28 yr time interval suggest positional shifts of between 0.5″ and 2.0″, implying proper motions of 0.02″–0.07″ yr^{-1}. These values are in basic agreement with previous proper motion estimates but are several times less than the expected $\approx$0.20″ yr^{-1} proper motion if 3C 58 is associated with SN 1181 and thus only 825 yr old.

5. Low-dispersion spectra of 463 individual knots (see Fig. 26) firmly establish the shock nature of the remnant's optical knots and filaments. Measured [S II]/Hα ratios lie above the well established ratio value of 0.4 for shock heated gas.

6. Most optical knots exhibited strong [N II] $\lambda\lambda$6548, 6583 relative to Hα (i.e., [N II]/Hα $>$ 3.0). A few knots showed exceptionally strong [N II] emission, with [N II]/Hα ratios above 10, suggesting a relatively high N/H abundances at least several times solar.

7. Measured knot radial velocities reveal a strong bimodal distribution of expansion velocities. Two distinct kinematic populations of knots are seen; one with a peak expansion velocity of around 1100 km s^{-1} and the other expanding much more slowly, less than 250 km s^{-1}. The faster expanding population appears to form part of a thick shell of knots, in places incomplete, with an average velocity of 770 km s^{-1} and a spread of $\pm$155 km s^{-1}.

Virtually no intermediate-velocity material is seen near the center of the remnant (within 75″ of the pulsar).

8. A NW–SE band of high-velocity knots running across the center of the 3C 58 remnant suggests an expanding ring of ejecta. This NW–SE band of knots roughly marks a dividing line between most other blueshifted and redshifted, high-velocity emission knots, and we propose a strongly bipolar structure to explain the distribution of high-velocity knots. However, the orientation of this bipolar expansion is not in alignment with either the remnant's E–W bipolar radio nebula or the X-ray emission structures observed immediately around the central pulsar.

9. We interpret the higher velocity group as SN ejecta and the slower group as shocked circumstellar material (CSM). The remnant's interaction with surrounding CSM may account for the thermal X-ray component seen in the remnant's outermost regions. The similarity of [N II] line emission strengths in both high- and low-velocity knots suggests similar N/H abundances between SN ejecta and pre-SN mass loss material.

10. Neither our proper motion estimates or radial velocity measurements support an ≈800 yr age for the 3C 58 remnant. If our estimated knot proper motions reflect undecelerated 3C 58 knot motions over the lifetime of the remnant, we estimate an age of around 3000–4000 yr. Similarly, a 770 km s^{-1} average knot velocity, a 3C 58 distance of 3.0 kpc suggests an age of between 2700 and 3500 yr assuming no deceleration.

We wish to thank M. Hammell for help with the image processing and coordinate matching, L. Rudnick for sending his VLA radio image, P. Slane for sharing his *Chandra* X-ray image data, and the referee for helpful comments and suggestions.

REFERENCES

Becker, R. H., Helfand, D. J., & Szymkowiak, A. E. 1982, ApJ, 255, 557
Bietenholz, M. F. 2006, ApJ, 645, 1180
Bietenholz, M. F., Kassim, N. E., & Weiler, K. W. 2001, ApJ, 560, 772
Blair, W. P., & Long, K. S. 1997, ApJS, 108, 261
Blair, W. P., Long, K. S., Vancura, O., Bowers, C. W., Conger, S., Davidsen, A. F., Kriss, G. A., & Henry, R. B. C. 1992, ApJ, 399, 611
Bocchino, F., Warwick, R. S., Marty, P., Lumb, D., Becker, W., & Pigot, C. 2001, A&A, 369, 1078
Camilo, F., et al. 2002, ApJ, 571, L41
Chevalier, R. A. 2004, Adv. Space Res., 33, 456
———. 2005, ApJ, 619, 839
Clark, D. H., Murdin, P., Wood, R., Gilmozzi, R., Danziger, J., & Furr, A. W. 1983, MNRAS, 204, 415
Clark, D. H., & Stephenson, F. R. 1977, The Historical Supernovae (Oxford: Pergamon)
Cox, D. P., & Raymond, J. C. 1985, ApJ, 298, 651
Davidson, K., & Fesen, R. A. 1985, ARA&A, 23, 119
Downes, R. A., Webbink, R. F., Shara, M. M., Ritter, H., Kolb, U., & Duerbeck, H. W. 2005, J. Astron. Data, 11, 2
Duyvendak, J. J. L. 1942, PASP, 54, 91
Fesen, R. A. 1983, ApJ, 270, L53
———. 2001, ApJS, 133, 161
Fesen, R. A., Blair, W. P., & Kirshner, R. P. 1985, ApJ, 292, 29
Fesen, R. A., & Ketelsen, D. A. 1985, The Crab Nebula and Related Supernova Remnants, 89
Fesen, R. A., & Kirshner, R. P. 1980, ApJ, 242, 1023
———. 1982, ApJ, 258, 1
Fesen, R. A., Kirshner, R. P., & Becker, R. H. 1988, in IAU Colloq. 101, Supernova Remnants and the Interstellar Medium, 55
Fesen, R. A., Martin, C. L., & Shull, J. M. 1992, ApJ, 399, 599
Fesen, R. A., Shull, J. M., & Hurford, A. P. 1997, AJ, 113, 354
Goldoni, P., Musso, C., Caraveo, P. A., & Bignami, G. F. 1995, A&A, 298, 535
Gotthelf, E. V., Helfand, D. J., & Newburgh, L. 2007, ApJ, 654, 267
Green, D. A. 1986, MNRAS, 218, 533
———. 1994, ApJS, 90, 817
———. 2004, Bull. Astron. Soc. India, 32, 335
Green, D. A., & Gull, S. F. 1982, Nature, 299, 606
Green, D. A., & Scheuer, P. A. G. 1992, MNRAS, 258, 833
Hartigan, P., Morse, J., & Raymond, J. 1994, ApJ, 436, 125
Helfand, D. J., Becker, R. H., & White, R. L. 1995, ApJ, 453, 741
Huang, Y. L. 1986, BAAS, 18, 1043
Ivanov, V. P., Rakhimov, I. A., Smolentsev, S. G., Stankevich, K. S., & Finkelstein, A. M. 2004, Astron. Lett., 30, 240
Kirshner, R. P., & Fesen, R. A. 1978, ApJ, 224, L59
Kwitter, K. B. 1981, ApJ, 245, 154
Lawrence, S. S., MacAlpine, G. M., Uomoto, A., Woodgate, B. E., Brown, L. W., Oliversen, R. J., Lowenthal, J. D., & Liu, C. 1995, AJ, 109, 2635
Liu, J.-Y. 1983, Studies Hist. Nat. Sci. 2, 45
Malofeev, V. M., Malov, I. F., Malov, O. I., & Glushak, A. P. 2003, Astron. Rep., 47, 413
Massey, P., & Gronwall, C. 1990, ApJ, 358, 344
Mayall, N. U., & Oort, J. H. 1942, PASP, 54, 95
MacAlpine, G. M., Lawrence, S. S., Sears, R. L., Sosin, M. S., & Henry, R. B. C. 1996, ApJ, 463, 650
MacAlpine, G. M., McGaugh, S. S., Mazzarella, J. M., & Uomoto, A. 1989, ApJ, 342, 364
Monet, D. E. A., et al. 1998, The USNO-A2.0 Catalogue (Washington: USNO)
Murray, S. S., Slane, P. O., Seward, F. D., Ransom, S. M., & Gaensler, B. M. 2002, ApJ, 568, 226
Oke, J. B. 1974, ApJS, 27, 21
Page, D., Lattimer, J. M., Prakash, M., & Steiner, A. W. 2004, ApJS, 155, 623
Peimbert, M., & van den Bergh, S. 1971, ApJ, 167, 223
Polcaro, V. F. 2004, in 7th Oxford International Archaeoastronomy Conf., in press
Raymond, J. C. 1979, ApJS, 39, 1
Reynolds, S. P., & Aller, H. D. 1988, ApJ, 327, 845
Roberts, D. A., Goss, W. M., Kalberla, P. M. W., Herbstmeier, U., & Schwarz, U. J. 1993, A&A, 274, 427
Slane, P., Helfand, D. J., van der Swaluw, E., & Murray, S. S. 2004, ApJ, 616, 403
Slane, P. O., Helfand, D. J., & Murray, S. S. 2002, ApJ, 571, L45
Smith, N. 2003, MNRAS, 346, 885
Sollerman, J., Lundqvist, P., Lindler, D., Chevalier, R. A., Fransson, C., Gull, T. R., Pun, C. S. J., & Sonneborn, G. 2000, ApJ, 537, 861
Stephenson, F. R. 1971, QJRAS, 12, 10
Stephenson, F. R., & Green, D. A. 1999, Astron. Geophys., 40, 27
———. 2002, Historical Supernovae and Their Remnants (Oxford: Clarendon Press)
Stone, R. P. S. 1977, ApJ, 218, 767
Toor, A., & Seward, F. D. 1974, AJ, 79, 995
Torii, K., Slane, P. O., Kinugasa, K., Hashimotodani, K., & Tsunemi, H. 2000, PASJ, 52, 875
Trimble, V. 1968, AJ, 73, 535
Trimble, V., & Rees, M. 1970, Astrophys. Lett., 5, 93
van den Bergh, S. 1978, ApJ, 220, L9
———. 1990, ApJ, 357, 138
van den Bergh, S., Marscher, A. P., & Terzian, Y. 1973, ApJS, 26, 19
van der Swaluw, E. 2003, A&A, 404, 939
Wallace, B. J., Landecker, T. L., & Taylor, A. R. 1994, A&A, 286, 565
Weiler, K. W., & Seielstad, G. A. 1971, ApJ, 163, 455
Wilson, A. S. 1972, MNRAS, 157, 229
Wilson, A. S., & Weiler, K. W. 1976, A&A, 49, 357
Woltjer, L. 1972, ARA&A, 10, 129
Woltjer, L., Salvati, M., Pacini, F., & Bandiera, R. 1997, A&A, 325, 295
Wu, C.-C. 1981, ApJ, 245, 581
Wyndham, J. D. 1966, ApJ, 144, 459
Yakovlev, D. G., Kaminker, A. D., Haensel, P., & Gnedin, O. Y. 2002, A&A, 389, L24
Zanin, C., & Kerber, F. 2000, A&A, 356, 274